COMPUTER METHODS IN MATERIALS SCIENCE

2024, vol. 24, no. 1, 25–36
https://doi.org/10.7494/cmms.2024.1.0828

Capabilities of numerical simulation support for defect investigations in die forgings

Marek Hawryluk[1]*, Sławomir Polak[1], Łukasz Dudkiewicz[1,2], Jan Marzec[1], Magdalena Jabłońska[3], Maciej Suliga[4], Roger Tkocz[5], Grzegorz Korpala[6]

[1] Wroclaw University of Science and Technology, Department of Metal Forming, Welding and Metrology, Wroclaw, Poland.
[2] Schraner Polska sp. z o.o., Łęczyca, Poland.
[3] The Silesian Technical University, Department of Material Technologies, Gliwice, Poland.
[4] Czestochowa University of Technology, Faculty of Production Engineering and Materials Technology, Czestochowa, Poland.
[5] MAHLE Behr Poland, Ostrów Wielkopolski, Poland.
[6] Institut für Metallformung, TU Bergakademie Freiberg, Freiberg, Germany.

Abstract

The article concerns the use of the results of numerical simulations, primarily for the detection of defects in forged products identified at various stages, along with the analysis of the geometry of forgings and the way in which the material flows in tools. The work presents the results of measurements and analyses using numerical modelling based on computational packages dedicated to forging processes such as: QForm, Forge, etc., which are equipped with special functions that significantly facilitate analyses by both technicians and designers. These functions include: contact of the deformed material with the tool, flow line distribution, "trap" or "fold" functions for detecting forging defects, as well as other technological parameters and physical sizes, which are crucial in the case of a comprehensive analysis of the industrial die forging process. The novelty of the work is the presentation of the possibility of simultaneously combining many different non-destructive techniques and methods, e.g. results of FE simulations with 3D reverse scanning, minimizing interference in the industrial process. The research carried out allows for the thorough and rapid analysis of the correctness of the deformation of the forging material for selected forging processes, along with the presentation of methods for their prevention and solving various technological and engineering problems, which is particularly important in terms of reliability and production efficiency

Keywords: forging defects, FE modelling, hot forging process, special function in FEM packages

1. Introduction

The high competitiveness of producers of forged products observed recently means that the main factor determining the potential choice of a supplier of forgings (apart from the price, which is the main factor taken into account) is primarily the quality and dimensional and shape accuracy of the offered products (Liu G. H., et al., 2012). The quality of forgings is especially important as described by Dyja et al. (2004) in the case of typical forged products, and for heavy forging (Liu Y. et al., 2018). This is particularly important in the case of the automotive (Park & Kwon, 2016), aviation, and military industries, where

*Corresponding author: marek.hawryluk@pwr.edu.pl
ORCID ID's: 0000-0002-9338-4327 (M. Hawryluk), 0000-0003-4696-6006 (S. Polak), 0009-0000-0191-7687 (Ł. Dudkiewicz), 0000-0003-4127-3315 (J. Marzec), 0000-0002-3807-9266 (M. Jabłońska), 0000-0002-3182-7831 (M. Suliga), 0009-0006-7195-8998 (R. Tkocz), 0000-0001-5388-8582 (G. Korpala)

the requirements related to the accuracy and quality of forgings are at the highest level (Hawryluk et al., 2023). Hot die forging technologies are among the most difficult production techniques, especially in the case of precision forging processes (Douglas & Kuhlmann, 2000). It is a manufacturing method whose most crucial advantage from different types of die forging is a reduction in material waste (up to 70%) resulting from the minimization of flash (Gronostajski & Hawryluk, 2008) and the production of a finished product with minimal allowances for mechanical processing (Zuo et al., 2014). In general, forgings obtained in the precision forging process have good mechanical as well as operational properties and are characterized by high manufacturing accuracy and a narrow tolerance range (Behrens et al., 2009). On the one hand, due to its advantages, this technology is most often used to produce parts for the automotive industry from different steel materials, for the production of gears, connecting rods, worm gears, tripods, turbines, alternators and constant velocity joints (Shan et al., 2004). On the other hand, although these technologies are relatively well mastered, the correct production of forgings with complex geometry, and additionally meeting high requirements of dimensional and shape accuracy and quality, requires extensive experience from technicians, designers and operators of forging units (Dieter et al., 2003). The improvement and implementation of new forging projects, continuous improvements and optimizations of implemented technologies, as well as a large number of important factors and phenomena affecting the correctness of the entire process, as well as the interaction of these factors, make die forging processes one of the most difficult manufacturing processes to implement and analyze (Gronostajski et al., 2014). At each of the individual steps of forging technology, there is a risk of mistakes and defect development in the forging process. The literature states that the most common defects in forgings (lack of filling, curling and crimping) are the result of incorrect shapes (Politis et al., 2018) as well as improper positioning of the blank or forging (Vazquez & Altan, 2000). Other causes of defects in forgings may include: too low temperature of the input material, the use of too large deformations, poorly made tools, inaccurate removal of scale or underdeveloped technology (Banaszek & Stefanik, 2006). Therefore, the design of blanks and forgings is an important issue for improving product quality and reducing production costs related to material losses per flash as well as losses related to defected manufactured parts (Liu Y. et al., 2018). One of the greatest threats during the forging process are forging defects and imperfections (Rathi & Jakhade, 2014). The most common in terms of forging quality, but at the same time the easiest to diagnose (Hawryluk & Ziemba, 2018), are errors in the flow of the deformed material (Fig. 1a) and incorrect filling of the working blanks (Fig. 1b) as well as partial or complete lack of filling (Fig. 1c, d).

The consequences of defects in the form of incorrect flow or failure to fill the blank with the deformed material are often material curls (partially visible on the forging – Fig. 2a) and crimping, which can only be noticed during defectoscopic examination or under a microscope (Fig. 2b), and sometimes at a later stage of production, e.g. after heat treatment (Fig. 2c) or, in extreme cases, only after final mechanical treatment (Fig. 2d).

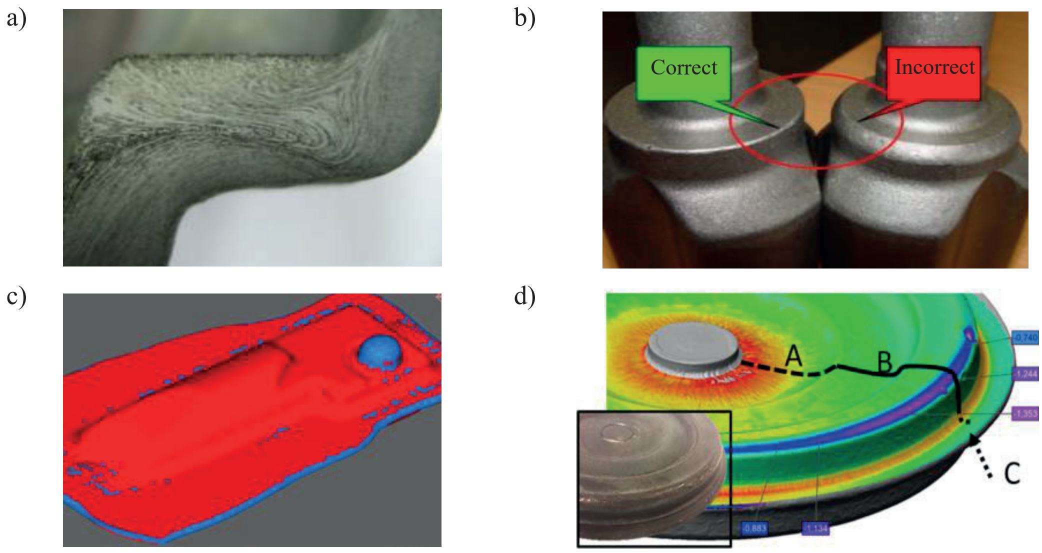

Fig. 1. Examples of forging flaws: a) improper material flow in the form of incorrect fiber distribution; b) failure to fill – no edge on the forging on the right side; c) FEM results – lack of filling in the area of the so-called “pin” in the forging of the window lock element; d) failure to fill part of the circumference in the forging of the front wheel disc

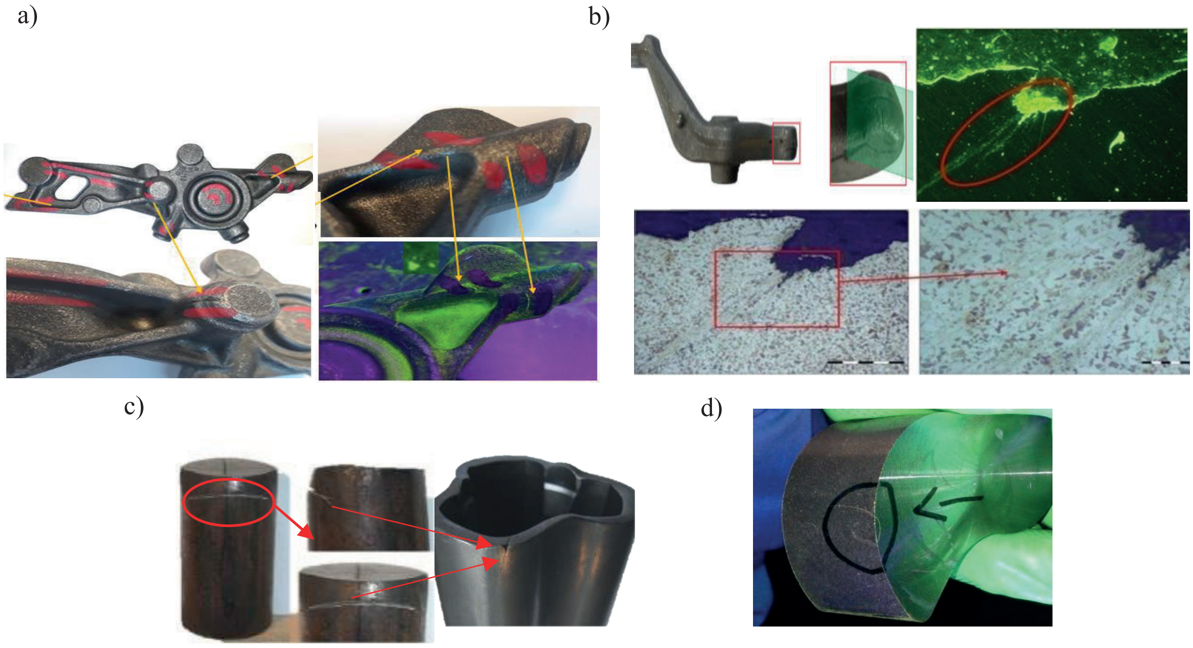

Fig. 2. Identification of exemplary defects in forgings: a) defect in the form of fold in the area of the pin and the tip of the elements in the forging of a drive lever for a sports motorcycle; b) forging photo in the head of the lever-type forging with marked defect (confirmed by defectoscope) – the microstructure with incorrect material flow; c) forging in the expander forging, revealed only after mechanical processing; d) a crack in the form of a fold revealed after mechanical treatment

The most difficult to detect and diagnose are folds/pressing areas, which are most often formed during poor material flow, when some of the deformed material still remains between the forging tools, creating bends which, in subsequent stages/operations, are pressed into the flash (Kumar et al., 2022). Also into the forging itself, which is unacceptable and causes disqualification of such elements from the process (Iwand & Wagner, 2010). Therefore, in order to design and improve the industrial forging process, a number of CAD/CAM/CAE tools are used, in particular numerical modeling and simulations, supported by IT techniques or measurement systems, like: coordinate-measuring machine, 3D scanners, advanced devices, others (Gronostajski et al., 2016). The use of numerical programs using both FEM and FVM to analyze issues related to incorrect geometry and/or positioning of the blank is currently the most common solution used by forges. The most popular and eagerly used programs are: Forge (Forge, n.d.), QForm (QForm UK, n.d.), SimufactForming (Simufact, 2015), etc. Currently, they are equipped by software producers with newer and newer functions enabling even more accurate analysis of bulk metal forming processes (Lu et al., 2018), enabling not only the basic technological parameters, although difficult to determine in any other way, or physical quantities: material flows, forces, strain distributions, temperature fields, etc. (Mohammadi & Sadeghi, 2009), but also more advanced ones, such as contact or the detection of flaws in forging elements, or even analysis of tooling durability after a specified number of forging cycles (Hawryluk et al., 2021). The use of these functions by an experienced user allows to significantly shorten the time needed to complete a new project and eliminate errors in instrumentation design. An example of one such special feature is the ability to analyze distances of the deformed forging material from the surface of the tool blank (contact) or forgings based on the "folds" function. This function works on the principle of lines on the surface of the forging, which expand and penetrate deeper during simulation, which, if they overlap, treat the situation as folding or crimping and enable accurate tracking of this defect, determining its size and depth and locating places formation of forges, their growth and final geometry with high accuracy (depending on the adopted size of the initial mesh and remeshing). Numerical modeling programs also enable the detection of air pockets ("trap" function), i.e. empty areas between the forging and the tool in which air is retained in the form of surface or volume. If this type of "trap" defect is detected, the computational solver determines the pressure in this area is based on the volume enclosed in this place and thus takes it as the initial boundary condition during numerical simulations, thus affecting the flow of the deformed material and the correct filling of the forging tool cavity (Hawryluk & Jakubik, 2016). Air pockets may cause gaps in the die cut, as well as premature destruction of dies by increased pressures in these surfaces. Therefore, further development and use of numerical modeling using new and very useful functions, such as contact, trap or folds, is fully justified both from the scientific and economic perspective due to the possibility of designing, comprehensive analysis and optimization of industrial forging processes, increasing thus, production efficiency and reliability (He, 2011).

2. Numerical detection of flaws and defects in the forged products

Currently, in order to analyze the correct flow of the deformed material and the appearance of possible flows in forged parts, the aforementioned FE modelling is mainly applied. This concept is based on more or less advanced functions that allow for the detection or prediction of a defect in the process.

2.1. The use of contact functions in numerical simulations

Contact detection in FEM is often used to analyze the correct flow of the deformed material and the degree of filling of the press forging die's working impression. Figure 3 shows the results of numerical modeling for the three-operation process of forging a 60E1A needle rail into a 60E1 rail profile.

The presented results of numerical simulations indicate in which areas the material did not flow or flowed incorrectly. In the analyzed case, these are mainly areas in red/yellow color, where the distance of the forged material to the surface of the cutout exceeds 2 mm (Fig. 3a). In next, both upper drawings present are places where there was no deformation due to the lack of a tool, therefore they are marked in red color. Figure 3b shows an enlargement of the zones of the forged end, where it can be clearly seen that the material did not fill the die working cavity. But gaps visible at the end of the forging of the needle rail are not a problem because it is contained in the part cut off (in the industrial process after forging) with a length of 100–150 mm. A more significant problem in this case is the lower part of the rail (foot), because the lack of material in this area causes the disqualification of such an element. Similarly, the contact function was used in the simulation of forging a geometrically complicated hinge-type element. The simulation of manufacturing a forging consists of 4 stages: bending and flattening on an MPM6300 hammer, followed by roughing and finishing forging on an MPM16000 hammer. Figure 4 presents the results of the impression filling in the operations: roughing and finishing forging.

The results obtained show that although no proper filling within the pin area was obtained in the roughing operation (area marked with red), the filling was correct in the finishing forging operation as that area was the closest to the die parting and it was deformed first in the finishing forging operation.

Similarly, in the case of another forged element – forgings with a transverse axis in a 6-fold arrangement (a window lock forging), an analysis of the regularity of deformation and the amount of filling of the blank by the deformed forging material was carried out using the contact function. The contact detection function was applied, where Figure 5a shows the final phase of filling (0.3 mm before full contact). In turn, in Figure 5, a complete filling of the impression is shown.

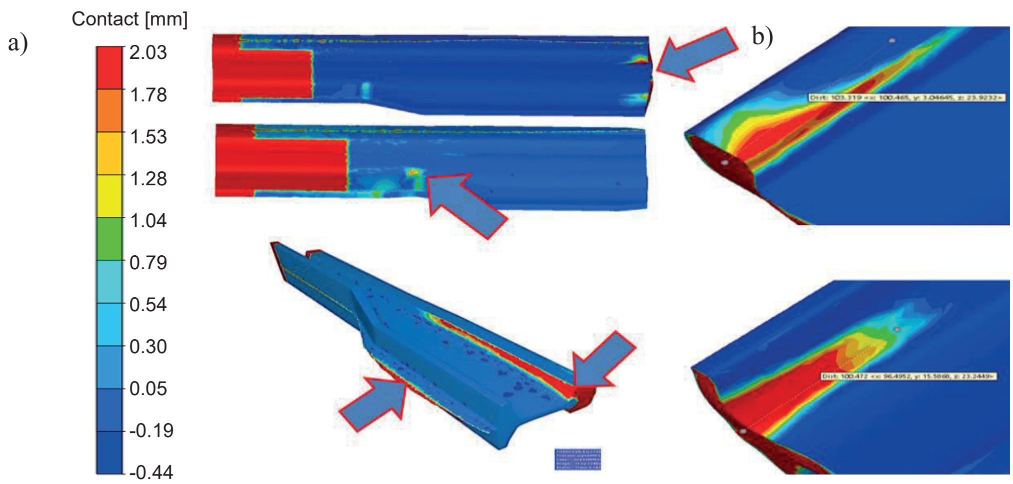

Fig. 3. The results of numerical simulation for the contact: a) at the end of deformation in final operation; b) image of enlarged areas with detected imperfections in the foot and head of the needle rail forging

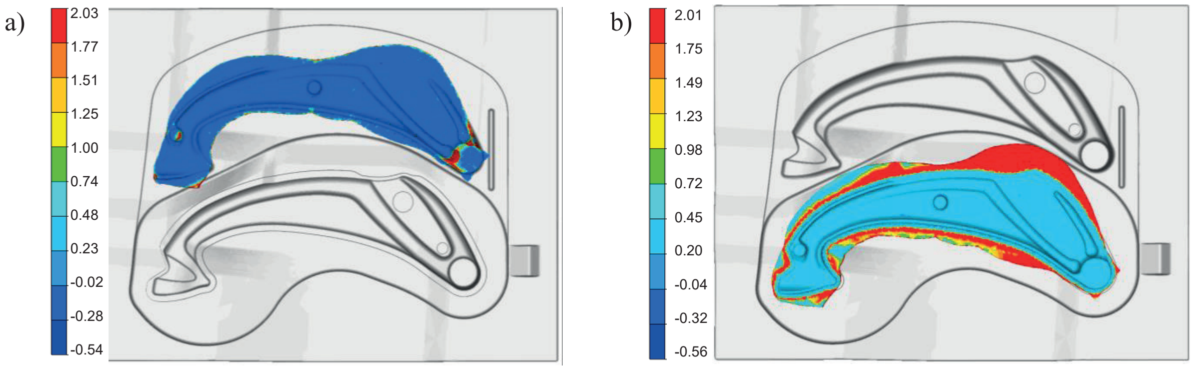

Fig. 4. The FEM results of material flows and filling cavity presented as the contact function: a) the roughing operation; b) the finishing forging operation

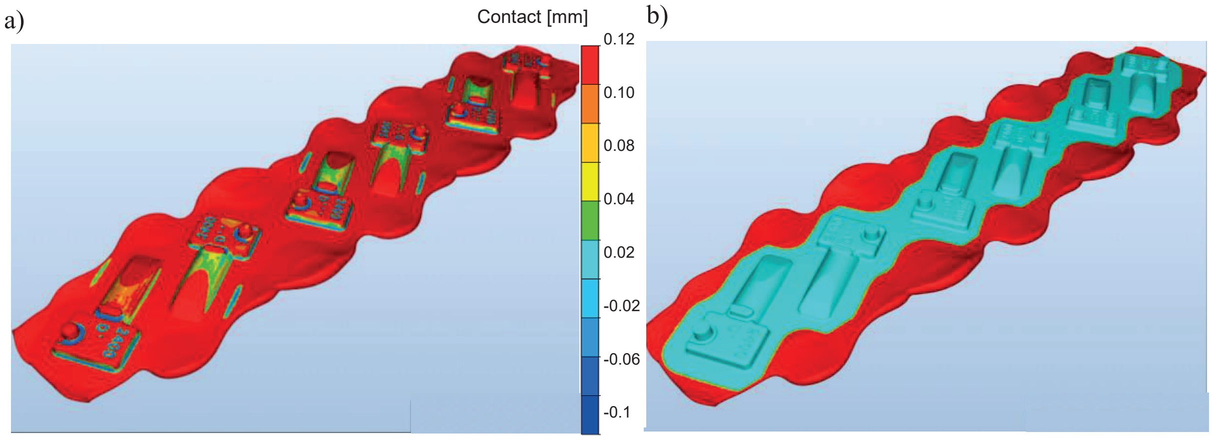

Fig. 5. FE results for finishing operation, with contact function deformed material with tools: a) 0.5 mm to full contact; b) end of the forging process

By means of this function, one can thoroughly analyse which areas in the forging are still deforming and flowing and which are no longer doing so. Such an analysis makes it possible to predict whether the deformed material is flowing according to the predictions or whether corrections are required.

2.2. The use of subsurface line functions to analyze the flow of the deformed forging material

A frequently used function in numerical simulations that facilitates the analysis of the flow of deformed material is the so-called subsurface lines or flow lines. Before the simulation, lines are introduced in the feed material in a rectangular arrangement in one or both directions. Then, during the simulation, the lines deform, showing the flow of the material. Figure 6 shows the results of modeling using flow lines for the deformed material of a tow hook forging intended for passenger cars towing trailers.

Surface lines were also used to analyze the way the material flowed during the forging process of a geometrically complex motorcycle lever type-forging (Fig. 7).

Figure 7 presents the results of deformed flow lines implemented into the feed material as a grid in both perpendicular directions. The FEM results regarding the distribution of fibers in the formed material confirm that defects (overlaps) may appear in the analysed zones. This is especially visible in area no. 2, i.e. in the recess, where one can see that the fibers from both directions have a high tendency to cross and bend. The results from the analysis of subsurface lines are similar for a fork-type forging in a double system. In Figure 8a one can see the line near the die dividing plane. There is continuity from the shoulder of the forging through the rear part, with no clear indications of cutting individual elements. Figure 8b, presents a similar correct way of arranging the flow lines in the protrusion of the forging. Additionally, when combining the obtained results with the Gartfield function, according to which the value is >0.8, a defect may occur.

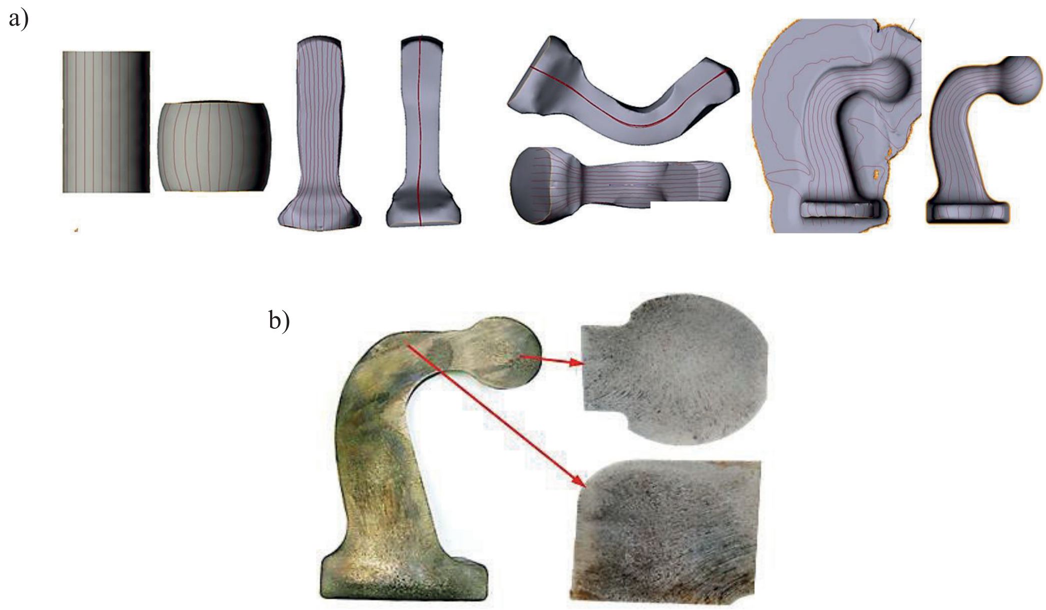

Fig. 6. FEM results of the correctness of deformation for the forging of a hook type forging: a) material flow lines for individual manufacturing operations; b) fiber distributions in the forging obtained as a result of the Jacewicz test

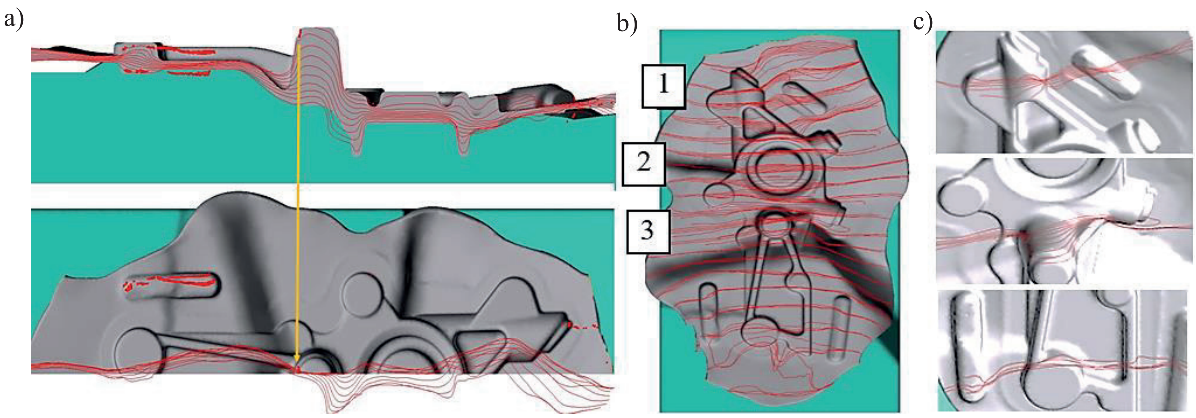

Fig. 7. The FE modelling results: a) the material flows with a distribution of flow lines in longitudinal; b) arrangement of fibers in the opposite direction; c) magnification for analysed zones 1–3

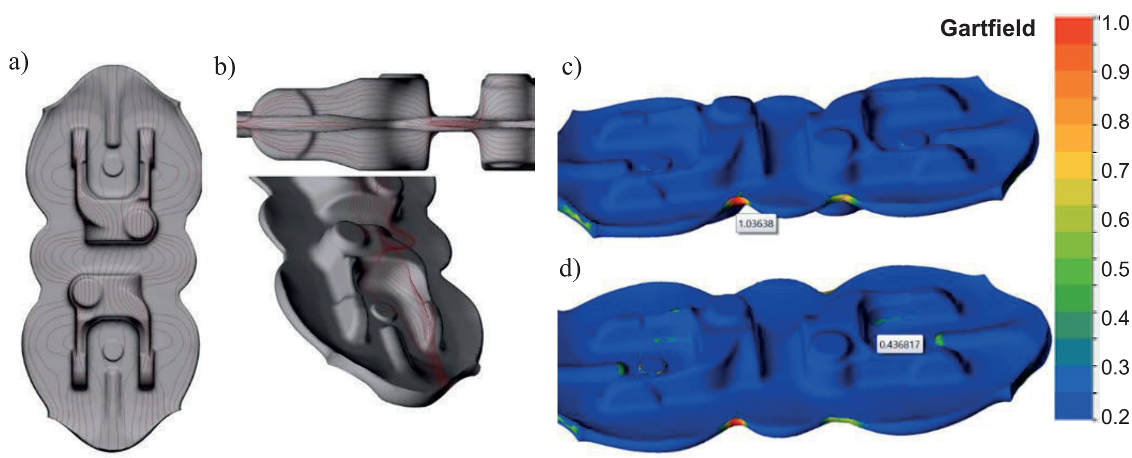

Fig. 8. Analysis of the subsurface (flow) lines of the forging during preliminary forging: a) lines around the dividing plane; b) flow lines in the plane of the arm zone; c) value of the Gartfield coefficient of the forging during preliminary forging in a double system; d) the results of Gartfield coefficient at the end of the process

Figures 8a and 8b show the flow line distribution for a fork forging produced in a double system. In turn, Figure 8c shows the place where the highest value of the Gartfield coefficient occurs in the place of material deficiency in the flash, which is permissible because there is still 1.8 mm left to completely fill (touch the dies). However, at the end of the forging process (Fig. 8d), there is no visible risk in the marked area, because the highest Gartfield values are 0.45 and occur on the arms, where they do not cause a risk of defect. It should be taken into account that when using the Gartfield criterion, the dimensional and shape tolerance values for a given forging should be taken into account, because it is on this basis that it is possible to determine what type of defect it is. Finally, one should also be aware that these are the results of numerical modeling and should be confirmed in reality.

2.3. FEM with a trap function to detect "air pockets"

A more advanced analysis function in calculation packages based on FE modeling is the so-called trap function, which enables the prediction of defects in the deformed material based on air pockets. Also, as result of an under-developed technology or its improper implementation (underheated tools or an excess of the lubricant, which has not managed to evaporate from the surface of the impression), it is possible to notice the possibility of a defect in the form of under-filling the tool cutout (Fig. 9a) in the process of manufacturing a yoke forging or a crank forging (Fig. 9c). The use of FEM numeral modelling with an active "trap" function for the detection of air pockets by means of the Forge program showed that, during the roughing operation, between the forging and the tool, a series of empty spaces containing air and the lubricating agent is formed (Fig. 9b).

Similarly, in the case of a crank-type forging, one can notice that so-called "air pockets" may be formed in the lowest areas of the tool impression and which reveal themselves in the form of underfills. Moreover, in both analyzed cases, an increased pressure value caused by the presence of an air pocket in this area can not only lead to a forging defect, but it can also damage the tools, thus accelerating the occurrence of microcracks and causing the so-called Rehbinder effect.

The "contact" function, in combination with the "trap" function, was used to analyze the failure to fulfil the so-called pins, i.e. small, conical areas in forgings that constitute elements of a window lock. Figure 10 shows the results of numerical simulations for the forging process of such elements in a multiple system. Figure 10a shows the results using the contact function in the final phase of the process. In turn, Figure 10b shows the results using the trap function, illustrating unfilled volumes in the analyzed areas.

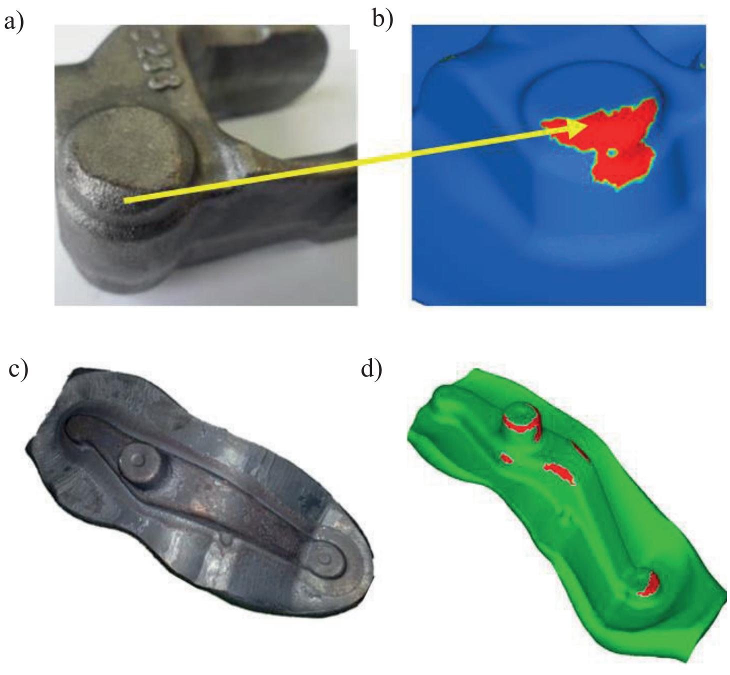

Fig. 9. The view of: a) failure of the forked type forging the real forging with defect of underfilling; b) results of FE modelling (the unfilled area marked with red) by use of the trap function; c) photo of a lever forging; d) visible laps in FEM

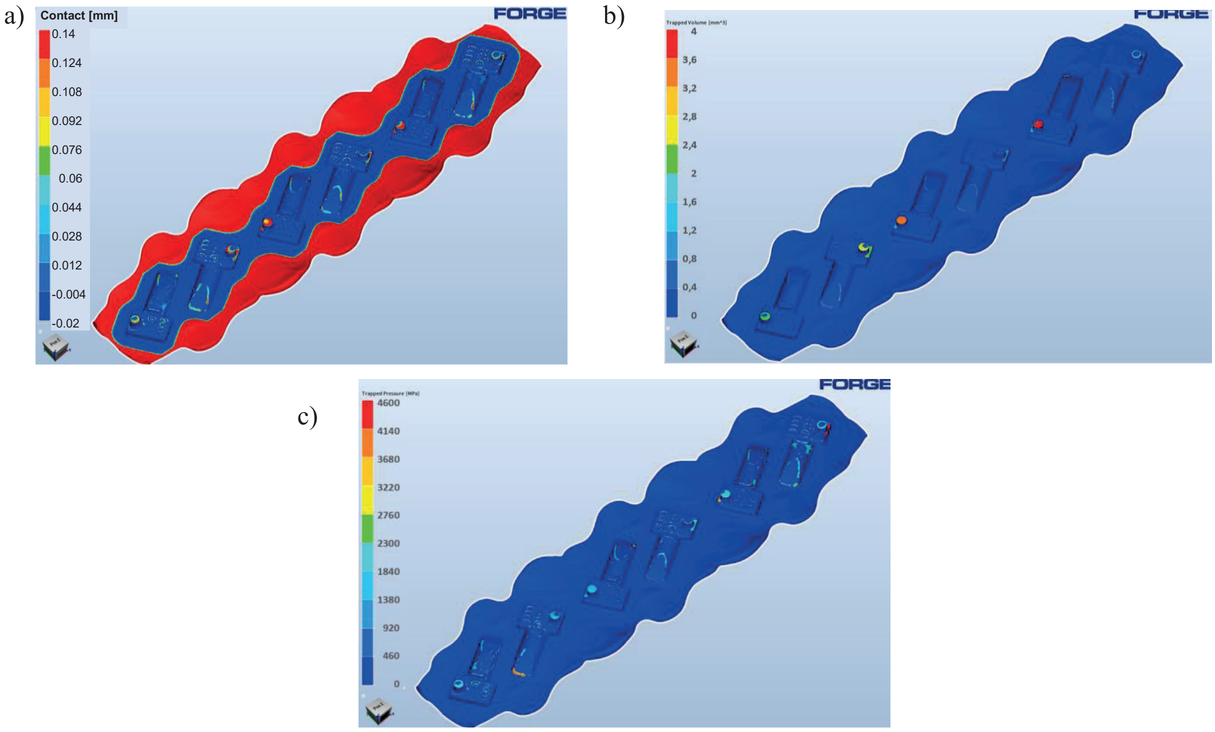

Fig. 10. FE rresults with the special functions – air pockets:
a) filling of the pins's cavities – contact during the end of the process; b) trapped and underfilled volumes;
c) distribution of the pressure field during the final phase of the forging process

In turn, Figure 10c shows how high the pressures are generated in these areas, which, on the one hand, may make it difficult to fill the blanks and, on the other hand, cause tools to break.

2.4. The use of the folds function – folds and laps of material

Defects of the deformed forging in the form of laps can be identified with the use of the folds function, where the laps are visible in the postprocessor as a cloud of red dots (spots). The use of the folds function is very helpful in analyzing this type of defects, because it allows to easily and quickly identify the area in the forging where a defect is likely to appear in the industrial process. For example, in the analyzed process of the initial forging of an element, such as a fork for the drive system of excavators (Fig. 11), there is a tendency for some parts of the deformed material to flow out of the shape of the blank, so the defects do not affect the parameters of the product.

However, in the case of the inexperience of the blacksmith operator and inappropriate manipulation and arrangement of the forging in the initial and finishing blanks, this may contribute to the occurrence of defects also in the forging, which unfortunately causes significant problems (Fig. 11).

Figure 12 shows the subsequent stages of forming using the folds function, thanks to which it is possible to analyze the flow of the material and the formation of possible defects on an ongoing basis.

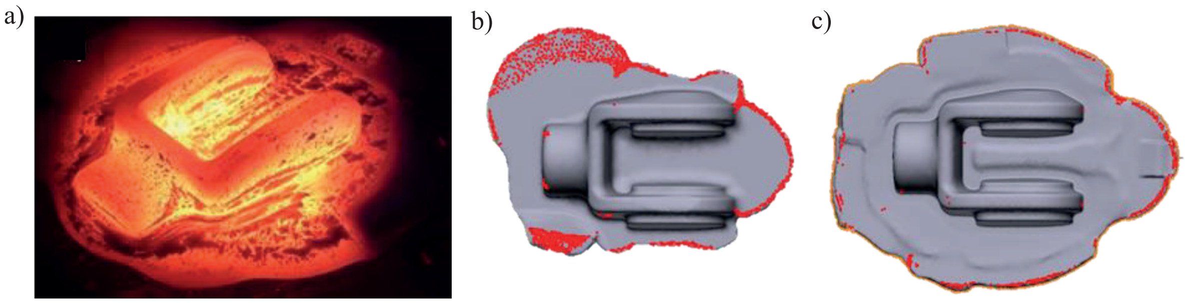

Fig. 11. Exemplary results of detection of forging defects:
a) the photo of hot forging; b) wrong arrangement of the die (too high) – laps on the arms;
c) too flat end (laps on the corners and the mandrel)

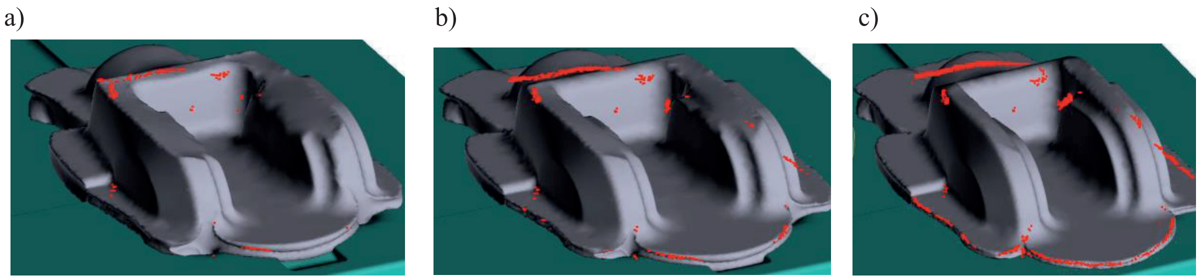

Fig. 12. Results of numerical modelling of fork type forging – the consecutive deformation phases: a) at the beginning; b) in the middle of deformation; c) at the end of forming

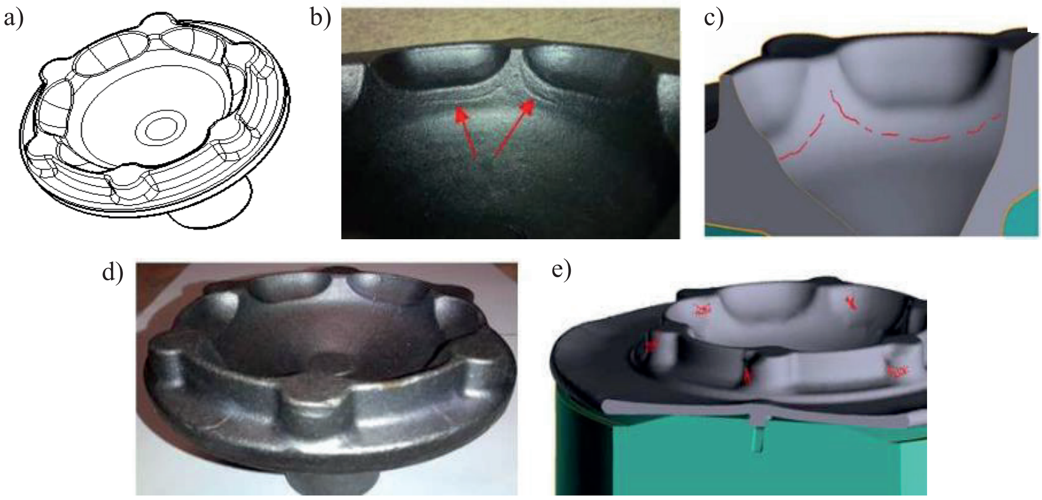

Fig. 13. Example results of detecting defects in forgings:
a) model of a hub-type forging; b) forgings and reflections in the forging; c) results of defect modeling;
d) forgings on the front surface; e) FEM – rotational displacement of tools in the axis

A similar situation with flaws in the form of folds was observed in the hot forging process of a very important element, such as the hub, which is intended for the drive systems of passenger cars (Fig. 13).

A defect in the form of a chisel/groove was observed (marked by arrows in Fig. 13b), which may also be caused by incorrect tool geometry (Fig. 13c). Another defect in the form of crimping was sometimes observed in the process and which was caused by the incorrect orientation of the upper tool relative to the lower one (Fig. 13d, e). Therefore, the use of special fold functions allows to simulate various arrangement variants and detect the areas of the formed material that are most vulnerable to defects.

2.5. Application of FE modelling to measurements of geometrical features of the forged parts

Combining numerical modeling with other IT tools or methods now gives even better results and allows for a more complete analysis. For example, using measurement techniques, e.g. based on scanning combined with 3D analysis, it is possible to mutually verify the developed numerical model (simulation results) and the geometry of forgings as nominal CAD models or forgings obtained from an industrial process. Figure 14 shows a comparison of the geometry and dimensional deviations map for the 60E1A6 rail profile, calculated numerically, with the developed nominal CAD model, which in this case allows the detemrination of the correctness of the assumptions made in the numerical modeling of the accurate forging process of needle rails used in railway turnouts.

Another, similar example of the simultaneous use of the results of numerical modeling and 3D scanning techniques may be the analysis of the trimming process of a forked type forging. Figure 15a presents the results of numerical simulation tests for the production process with worn forging and trimming tools as a comparison of the FE results after the forging and trimming processes. In turn, Figure 15b shows the scanning results of forging without flash from an industrial forging process (and trimming) in comparison to the nominal CAD model.

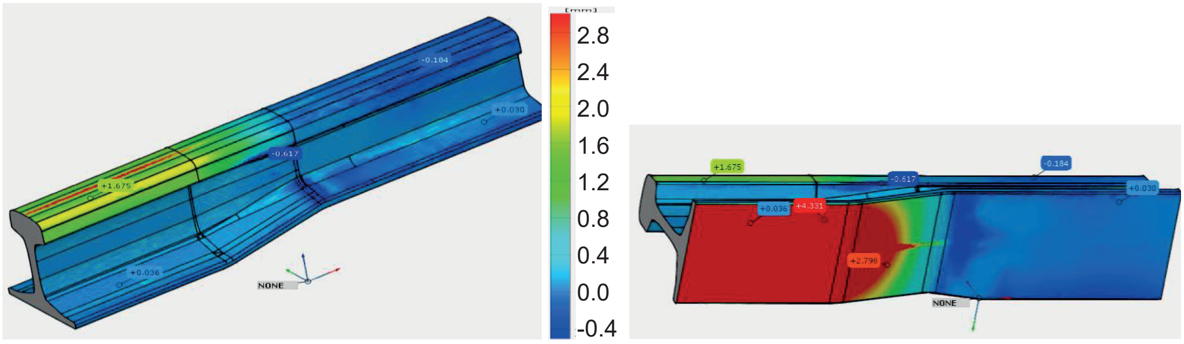

Fig. 14. Comparison of geometry calculated from FEM to the nominal shape and dimensions from the CAD model for needle rails used in railway turnouts

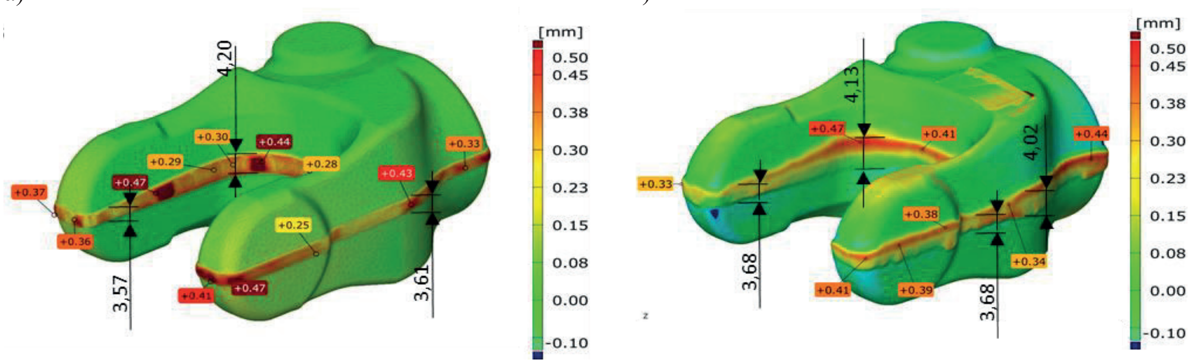

Fig. 15. A comparison of a FE forging model after forging and trimming of the flash with colour maps of deviations in a normal direction and cutting edge thickness: a) results of FEM in relation to nominal CAD; b) results of industrial process realised in similar real conditions (a scan of real forging to CAD model)

The comparison results obtained indicate that both the geometry and deviations in the trimming zone (cutting line) for the forging obtained from FEM and for the forging obtained in an industrial process for similar conditions are highly similar. This is evidenced by, among others, the results of the width of the cutting line, which for the numerical model is in the range of 2.00–3.11 mm, and the deviations in the normal direction are 0.11 mm to 0.30 mm. It is similar in the case of a forging obtained for such conditions in a real process. However, both the line width (from 2.00 mm to 3.41 mm) and deviations in the normal direction are more diverse along the cutting lines (0.10 mm to 0.25 mm). This can be explained by the fact that numerical modelling is carried out in ideal "virtual" conditions in relation to the industrial process, in which factors affecting the final geometry of the forging may occur.

The results of numerical simulations combined with scanning techniques can also be used to analyze the progressive wear of the forging die based on scanning of cyclically sampled forgings from the industrial process, as well as the impact of destructive mechanisms on possible defects in the forgings (Fig. 16). Based on the distribution of equivalent (the highest value over 1,200 MPa) and normal stresses (value about 1,100 MPa), it is possible to predict which areas of the tool are most exposed to wear. At the same time, based on these most loaded areas, it is possible to draw conclusions about similar areas in forgings in which the greatest changes in geometry will occur. The maximum value of material loss/increase is in the same areas, both in tool and forging, but for a die one can observe a loss of material with a value about −0.15 mm. At the same time for forging one can see an increase of material (+0.13 mm). The production process should be interrupted if such changes exceed the permissible tolerance range.

Based on the presented results and conducting long-term analyses, it becomes possible to use changes in the geometry of forgings to map them in the working blanks of tools and then model the process for such conditions in FEM. In this way, numerical modelling is possible, and the results are even closer to genuine industrial conditions.

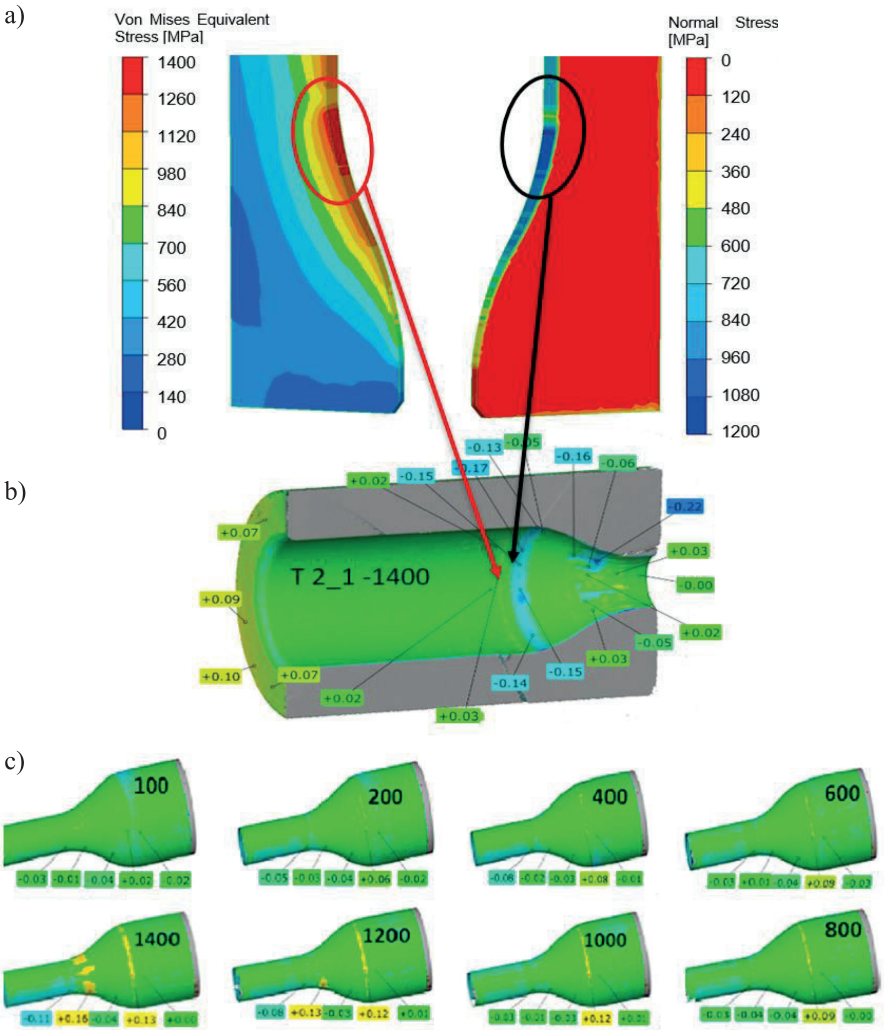

Fig. 16. Analysis of the operation of the forging tool and forgings: a) results of numerical simulations with the distribution of equivalent stresses and normal pressures in the tools; b) results of scanning the used die; c) scans of forgings periodically taken from the process (Hawryluk, 2021)

3. Summary

The article presents the results of a mumber of years of scientific research on the possibility of using mainly numerical simulations to analyze and detect defects in forgings and eliminate them. The use of computational packages not only made it possible to carry out relatively simple analyzes of forging processes, but also measurements and analysis of process correctness in order to determine key technological parameters, such as forging force patterns, temperature and strain field distributions, i.e. typical analyzes and process optimization. Additionally, the use of more advanced functions, such as: contact lines, flow lines, or the Gartfield criterion, as well as others, such as the appearance of air pockets and crimps, allow the detection and prediction of defects in forged products. It should be emphasized, as shown in the final part of the article, that the best results and most comprehensive analysis are obtained by combining and using many methods at the same time, such as: numerical modeling with 3D scanning. Combined FE modelling with scanning techniques can also be used to analyze the progressive wear of the forging dies, as well as allowing for the prediction of defects in the forgings.

Based on the presented results one can observe the vast potential of this type of numerical tools and IT techniques for applications in the forging industry, because they can significantly shorten analysis time and the measurement of key parameters. They also provide a lot of valuable information and physical quantities that are difficult to determine analytically or experimentally. This means that a virtual experiment using all these methods allows for a significant reduction in the costs associated with carrying out research and the development of a technology in an industrial processes.

References

Banaszek, G., & Stefanik, A. (2006). Theoretical and laboratory modelling of the closure of metallurgical defects during forming of a forging. *Journal of Materials Processing Technology*, *177*(1–3), 238–242. https://doi.org/10.1016/j.jmatprotec.2006.04.023.

Behrens, B.-A., Nickel, R., & Müller, S. (2009). Flashless precision forging of a two-cylinder-crankshaft. *Production Engineering-Research and Development*, *3*(4–5), 381. https://doi.org/10.1007/s11740-009-0185-x.

Dieter, G. E., Kuhn, H. A., & Semiatin, S. L. (2003). *Handbook of Workability and Process Design*. The Materials Information Society.

Douglas, R., & Kuhlmann, D. (2000). Guidelines for precision hot forging with applications. *Journal of Materials Processing Technology*, *98*(2), 182–188. https://doi.org/10.1016/S0924-0136(99)00197-1.

Dyja, H., Banaszek, G., Berski, S., & Mróz, S. (2004). Effect of symmetrical and asymmetrical forging processes on the quality of forged products. *Journal of Materials Processing Technology*, *157–158*, 496–501. https://doi.org/10.1016/j.jmatprotec.2004.07.109.

Forge (n.d.). Retrieved from http://www.kc96.pl.

Gronostajski, Z., & Hawryluk, M. (2008). The main aspects of precision forging. *Archives of Civil and Mechanical Engineering*, *8*(2), 39–55. https://doi.org/10.1016/S1644-9665(12)60192-7.

Gronostajski, Z., Kaszuba, M., Hawryluk, M., & Zwierzchowski, M. (2014). A review of the degradation mechanisms of the hot forging tools. *Archives of Civil and Mechanical Engineering*, *14*(4), 528–539. https://doi.org/10.1016/j.acme.2014.07.002.

Gronostajski, Z., Hawryluk, M., Jakubik, J., Kaszuba, M., Misiun, G., & Sadowski, P. (2016). Solution examples of selected issues related to die forging. *Archives of Metallurgy and Materials*, *60*(4), 2767–2775. https://doi.org/10.1515/amm-2015-0446.

Hawryluk, M., & Jakubik, J. (2016). Analysis of forging defects for selected industrial die forging processes. *Engineering Failure Analysis*, *59*, 396–409. https://doi.org/10.1016/j.engfailanal.2015.11.008.

Hawryluk, M., & Ziemba, J. (2018). Application of the 3D reverse scanning method in the analysis of tool wear and forging defects. *Measurement*, *128*, 204–213. https://doi.org/10.1016/j.measurement.2018.06.037.

Hawryluk, M., Ziemba, J., Zwierzchowski, M., Janik, M. (2021). Analysis of a forging die wear by 3D reverse scanning combined with SEM and hardness tests. *Wear*, *476*, 203749. https://doi.org/10.1016/j.wear.2021.203749.

Hawryluk, M., Gronostajski, Z., Jabłoński, P., Janik, M., & Suliga, M. (2023). An integrated vision control system for the evaluation of the shape-dimensional accuracy and quality of valve forgings used in motor truck engines. *Measurement*, *210*, 112541. https://doi.org/10.1016/j.measurement.2023.112541.

He, X. (2011). Effects of manipulator compliant movements on the quality of free forgings based on FEM simulation. *The International Journal of Advanced Manufacturing Technology*, *56*(9–12), 905–913. https://doi.org/10.1007/s00170-011-3253-2.

Iwand, H. C., & Wagner, J. W. (2010). Failure analysis of open end wrenches containing forging defects. *Journal of Failure Analysis and Prevention*, *10*(6), 520–524. https://doi.org/10.1007/s11668-010-9371-6.

Kumar, S., Babasaeb, K. A., & Dipak, K. S. (2022). An overview of forging process and defects in hot and cold forging. *International Research Journal of Engineering and Technology (IRJET)*, *9*(7), 121–129.

Liu, G. H., Zhuang, Z., Liu, P., Ni, L. Y., Zhu, S. Y., Chen, J. J., Lin, Ch. H., & Liu, L. H. (2012). Influence of the blooming processes of heavy forgings on the forgings quality. *Advanced Materials Research*, 538–541, 1067–1071. https://doi.org/10.4028/www.scientific.net/AMR.538-541.1067.

Liu, Y., Wu, J., Wang, D., & Liu, S. (2018). Defect analysis and design optimization on the hot forging of automotive balance shaft based on 3D and 2D simulations. *International Journal of Advanced Manufacturing Technology*, *94*, 2739–2749. https://doi.org/10.1007/s00170-017-1080-9.

Lu, B., Ou, H., & Long, H. (2011). Die shape optimisation for net-shape accuracy in metal forming using direct search and localised response surface methods. *Structural and Multidisciplinary Optimization*, *44*(4), 529–545. https://doi.org/10.1007/s00158-011-0635-x.

Mohammadi, M. M., & Sadeghi, M. H. (2009). Simulation and physical modelling of forging sequence of Bj type outer race. *Advanced Materials Research*, *83–86*, 150–156. https://doi.org/10.4028/www.scientific.net/AMR.83-86.150.

Park, D.-H., & Kwon, H.-H. (2016). Development of automobile engine mounting parts using hot-cold complex forging technology. *International Journal of Precision Engineering and Manufacturing-Green Technology*, *3*(2), 179–184. https://doi.org/10.1007/s40684-016-0023-5.

Politis, D. J., Politis, N. J., & Dean, T. A. (2018). A review of force reduction methods in precision forging axisymmetric shapes. *International Journal of Advanced Manufacturing Technology*, *97*(5–8), 2809–2833. https://doi.org/10.1007/s00170-018-2151-2.

QForm UK (n.d.). Retrieved from https://www.qform3d.com.

Rathi, M. G., & Jakhade, N. A. (2014). An overview of forging processes with their defects. *International Journal of Scientific and Research Publications*, *4*(6), 112–117.

Shan, D. B., Xu, W. C., & Lu, Y. (2004). Study on precision forging technology for a complex-shaped light alloy forging. *Journal of Materials Processing Technology*, *151*(1–3), 289–293. https://doi.org/10.1016/j.jmatprotec.2004.04.075.

Simufact (2015). *Simufact forming reference manual 15.0*.

Vazquez, V., & Altan, T. (2000). New concepts in die design – physical and computer modeling applications. *Journal of Materials Processing Technology*, *98*(2), 212–223. https://doi.org/10.1016/S0924-0136(99)00202-2.

Zuo, B., Wang, B. Y., & Yang, L. Y. (2014). Forming load calculation of hot precision forging of cylindrical gears. *Applied Mechanics and Materials*, *456*, 425–428. http://doi.org/10.4028/www.scientific.net/AMM.456.425.

COMPUTER METHODS IN MATERIALS SCIENCE

2024, vol. 24, no. 1, 37–49
https://doi.org/10.7494/cmms.2024.1.0826

Plastic deformation mechanisms in BCC single crystals and equiatomic alloys: Insights from nanoindentation

Francisco Javier Dominguez-Gutierrez[1*], Stefanos Papanikolaou[1], Silvia Bonfanti[1], Mikko Alava[1,2]

[1] NOMATEN Centre of Excellence, National Center for Nuclear Research, 05-400 Świerk/Otwock, Poland.
[2] Department of Applied Physics, Aalto University, P.O. Box 11000, 00076 Aalto, Espoo, Finland.

Abstract

Deformation plasticity mechanisms in alloys and compounds may reveal the material's capacity towards optimal mechanical properties. We conducted a series of molecular dynamics (MD) simulations to investigate plasticity mechanisms due to nanoindentation in pure tungsten, molybdenum, and vanadium body-centered cubic single crystals, as well as the body-centered cubic, equiatomic, random solid solutions (RSS) of tungsten–molybdenum and tungsten–vanadium alloys. Our analysis focuses on a thorough, side-by-side comparison of dynamic deformation processes, defect nucleation, and evolution, along with corresponding stress–strain curves. We also checked the surface morphology of indented samples through atomic shear strain mapping. As expected, the presence of Mo and V atoms in W matrices introduces lattice strain and distortion, increasing material resistance to deformation and slowing down dislocation mobility of dislocation loops with a Burgers vector of 1/2 ⟨111⟩. Our side-by-side comparison displays a remarkable suppression of the plastic zone size in equiatomic W–V RSS, but not in equiatomic W–Mo RSS alloys, displaying a clear prediction for optimal hardening response of equiatomic W–V RSS alloys. If the small-depth nanoindentation plastic response is indicative of overall mechanical performance, it is possible to conceive a novel MD-based pathway towards material design for mechanical applications in complex, multi-component alloys.

Keywords: nanoindentation, alloys, hardness, machine learning interatomic potentials, dislocation dynamics, plasticity, tungsten

1. Introduction

Tungsten–Molybdenum (W–Mo) alloys are promising materials with superior physical properties. These alloys are suitable for sustaining extreme operating conditions without degradation (Chen Q. et al., 2021; Kramynin, 2022; Lan et al., 2022; Liu et al., 2013; Sahoo et al., 2015). As the W percentage increases, the thermal conductivity decreases while the strength at both room and high temperatures increases (Chen Q. et al., 2020; Jiang et al., 2018; Ohser-Wiedemann et al., 2013; Tao et al., 2022). In addition, Mo and W form isomorphic solid solutions due to their complete solid and liquid solubility, enabling the creation of solid solutions across the composition range (Gaffin et al., 2022; Lan et al., 2022; Wei et al., 2023). Nevertheless, it is known that tungsten exhibits relatively low fracture toughness at low temperatures, rendering it susceptible to cracking (Arshad et al., 2014; Gumbsch et al., 1998). As an alternative, the addition of vanadium to W matrices (W–V alloys) may enhance mechanical properties and improve creep resistance at elevated

* Corresponding author: javier.dominguez@ncbj.gov.pl

ORCID ID's: 0000-0002-1429-0083 (F.J. Dominguez-Gutierrez), 0000-0001-5239-1275 (S. Papanikolaou), 0000-0002-0323-8714 (S. Bonfanti), 0000-0001-9249-5079 (M. Alava)

temperatures (Jiang et al., 2019; Muzyk et al., 2011; Wei et al., 2023; Wurster et al., 2011). Furthermore, vanadium has recently been recognized as a unique element for strengthening in high entropy alloys and, more generically, random alloy solutions (Yin et al., 2020).

Nanoindentation simulations are capable of characterizing the mechanical response of materials under external loads at the nanoscale, particularly for their dislocation nucleation and evolution, as well as induced plastic patterning, referring to the creation of patterns or structures within the material (Domínguez-Gutiérrez et al., 2023; Varillas et al., 2017). It involves applying a small, sharp tip onto the material's surface, measuring the required force and the subsequent material displacement (Domínguez-Gutiérrez et al., 2021b; Kurpaska et al., 2022; Pathak & Kalidindi, 2015; Schuh, 2006; Varillas et al., 2017). This process finds various applications, such as developing nanostructured surfaces with enhanced functionalities and engineering materials with specific mechanical properties (Das et al., 2018; Li Z. et al., 2020). The plastic patterning resulting from nanoindentation is influenced by factors such as the applied load, material composition, and surface orientation. A deeper understanding of the material's deformation within the plastic zone beneath the indented surface region is essential for interpreting these effects (Mulewska et al., 2023a; Varillas et al., 2017; Wyszkowska et al., 2023).

In this work, we investigate the effects of vanadium in random solid solution W–based alloys, with a focus on the influence of varying vanadium concentrations on the morphology, densification, and mechanical properties, which have not been extensively studied in W-based alloys. (Wurster et al., 2011). Our aim is to gain insights into the behavior of alloys under external loads and explore the potential for developing novel material design methods. We achieve this by investigating nanoindentation-induced plasticity through load-displacement curves and surface patterning, as referenced in existing literature (Alcalá et al., 2012; Frydrych et al., 2023; Karimi et al., 2023; Oliver & Pharr, 1992; Schuh, 2006; Yu et al., 2020). Molecular dynamics (MD) simulations, particularly large-scale atomistic simulations, offer a cost-effective alternative for comprehending plastic deformation mechanisms in tungsten (W) and its alloys (Domínguez-Gutiérrez et al., 2021b, 2023; Kurpaska et al., 2022; Pitts et al., 2013; Varillas, 2019). The transition from elasticity to plasticity is characterized by pop-in events – sudden displacements indicating the initiation of dislocation sources in small indentation zones, as discussed in our work (Domínguez-Gutiérrez et al., 2023; Karimi et al., 2023; Pathak & Kalidindi, 2015; Pathak et al., 2014). This phenomenon highlights a distinct drop in stress, a focal point in our study of equiatomic W–Mo and W–V alloys' hardening properties compared to single elements (Li T. L. et al., 2011; Mulewska et al., 2023b; Naghdi et al., 2022; Pöhl, 2019; Xiong et al., 2016), despite maintaining the body-centered cubic (BCC) crystalline structure.

2. Computational methods

We performed computer simulations using the Large-scale Atomic/Molecular Massively Parallel Simulator (LAMMPS) (Thompson et al., 2022) and the Embedded atom model with Finis–Sinclair (EAM-FS) potential developed for W–Mo and W–V by Chen Y. et al. (2020). This potential accurately models various physical and mechanical properties, ⟨111⟩ dumbbell migration, stacking fault energies, and relative stability of the ⟨100⟩ and 1/2⟨111⟩ interstitial dislocation loops. While, the surface energies of these two metals are reported to be slightly lower than the DFT results. Supplementary Material (SM), we report the elastic constants (C_{ij}), bulk modulus [GPa], shear modulus [GPa], Poisson's ratio, and the Young's modulus (E_Y [GPa]) of single element samples of W, Mo, and V, as well as random equatomic samples of W–Mo and W–V alloys that are generated by randomly substituting W atoms by Mo or V.

For modeling nanoindentation, the initial BCC samples of W, Mo, and V were created with lattice constants of approximately 0.316 nm, 0.315 nm, and 0.303 nm, respectively. The sample dimensions were deliberately selected to accommodate the expected dislocation loop propagation along slip families. For the [001] orientation, the dimensions, (d_x, d_y, d_z), were approximately 50 nm × 50.56 nm × 51.19 nm, encompassing 8,190,720 atoms. Similarly, for the [011] orientation, the sample was sized at around 50.24 nm × 51.84 nm × 49.16 nm, comprising 8,115,360 atoms. In the case of the [111] orientation, the sample measured approximately 51.40 nm × 50.09 nm × 50.63 nm, housing 8,424,900 atoms. The x and y axes have periodic boundary conditions to simulate an infinite surface, while the z orientation has a frozen bottom boundary to avoid vertical translation and to assure stability of the atoms when nanoindentation is performed, a thermostatic section above the frozen layer to dissipate the heat generated during nanoindentation, and a "dynamical" section for atoms–indenter interaction allowing atoms to move freely, as shown in Figure 1. Additionally, a 5 nm vacuum region is added atop the sample as an open boundary (Domínguez-Gutiérrez et al., 2021b; Kurpaska et al., 2022).

The W–Mo and W–V alloys are created by random substitution of 50% of W atoms from the initial BCC W sample with Mo or V atoms, as done previously, an assumption supported by thermodynamic binary alloy phase diagram calculations (Dominguez-Gutierrez et al., 2022; Muzyk et al., 2011; Turchi et al., 2005). The FIRE (fast inertial relaxation engine) 2.0 protocol (Guénolé et al., 2020) is then used to optimize the samples' geometry towards the closest local minimum of energy structure. We consider the following criteria for the optimization process where the change in energy between successive iterations and the most recent energy magnitude is less than 10^{-5} and when the global force vector length of all atoms is less than or equal to 10^{-8} eV/Å. We observed a 0.09% reduction in the cell volume of the W–Mo alloy after the optimization process, while the W–V alloy exhibited a substantial 7.77% decrease. Additionally, the d_z size of the W–V sample underwent a notable 9.73% reduction. These changes reflect the impact of V atoms on the W matrix. The samples are initially equilibrated at T = 300 K for 2 ns using an isobaric-isothermal ensemble. This equilibration is achieved by integrating the Nose–Hoover equations with damping parameters, specifically, τ_T = 2 fs for the thermostat and τ_P = 5 ps for the barostat, while maintaining an external pressure of 0 GPa (Kurpaska et al., 2022; Xu Q. et al., 2023). This process continues until the system attains homogeneous temperature and pressure profiles. In Figure 1, we illustrate the atomic distribution of W and Mo on the surface, underscoring the necessity of conducting multiple nanoindentation simulations to ensure robust statistical outcomes in our study.

The indenter tip is defined as a non-atomic repulsive imaginary (RI) rigid sphere, exerting a force of magnitude $F(t) = K(r(t) - R_i)^2$ on each atom. Here, K = 236 eV/Å^3 denotes the specified force constant, ensuring a high stiffness for our indenter tip (Varillas et al., 2017). The parameter $r(t)$ represents the distance from the atoms to the center of the indenter, and R_i = 15 nm is the radius of the indenter, chosen sufficiently large to accurately model the elastic-to-plastic deformation transition. Given that EAM potentials tend to yield lower surface energies than those obtained via DFT calculations, they lack the capability to simulate interactions between the indenter tip and the atoms on the top surface layer, particularly when the tip radius is equal to or less than 5 nm, as observed in our previous work computing normalized maximum shear stress by the pressure applied (Domínguez-Gutiérrez et al., 2023; Xu Q. et al., 2023). The initial location of the tip is set at a separation distance of 0.5 nm from the material's surface, and its center is randomly shifted to ten different positions to account for statistical variation, as depicted by black dots in Figure 1. We employ an NVE statistical thermodynamic ensemble with the velocity Verlet algorithm for an indenter speed of v = 20 m/s for 125 ps, using a time step of Δt = 1 fs. A maximum indentation depth of h_{max} = 2.0 nm is selected to minimize boundary layer effects in the dynamic atoms region.

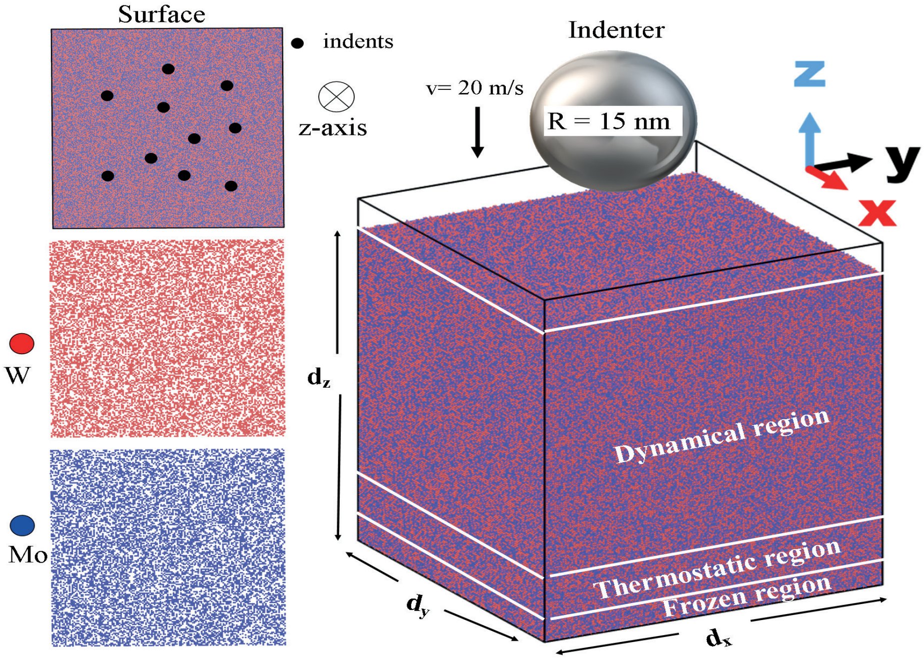

Fig. 1. Standard setup employed in our MD simulations for nanoindentation. The samples are partitioned into three regions to account for boundary conditions. We employ a non-atomic repulsive spherical indenter at a given strain rate. The target area configuration displays the random atomic distribution within the sample with black dots as indenter marks

3. Results

The common pathway to investigate nanoindentation is through average force-displacement curves, which gives the information to define the mean contact pressure p as (Johnson, 1987; Remington et al., 2014; Varillas, 2019):

$$p(h) = \frac{2\pi}{3E_Y}\left[24P_{ave}(h)\left(\frac{E_Y R_i}{1-\nu^2}\right)^2\right]^{1/3} \tag{1}$$

where h is the indentation depth, ν is the Poisson's ratio, and the average load is calculated as $P_{ave}(h) = 1/N\sum_i^N P_i(h)$ with $P_i(h)$ as the load from each MD simulation and $N = 10$ the number of indents. During loading process, the contact radius is obtained with the geometrical relationship (Domínguez-Gutiérrez et al., 2023):

$$a(h) = \left[3P_{ave}(h)R_i\frac{1-\nu^2}{8E_Y}\right]^{1/3} \tag{2}$$

Quantities $p(h)$ and $a(h)$ provide an intrinsic measure of the surface resistance to defect nucleation (Domínguez-Gutiérrez et al., 2023; Varillas et al., 2017) and yield to a universal linear relationship between $p(h)/E_Y$ and $a(h)/R_i$ given by:

$$\frac{p(h)}{E_Y} = \frac{0.844}{1-\nu^2}\frac{a(h)}{R_i} \tag{3}$$

Figures 2 and 3 show the ratio between $p(h)$ and the Young's modulus E_Y, for each sample, as a function of the normalized contact radius $a(h)/R_i$ between the sample and the tip. This is utilized to identify the pop-in event, where the contact pressure deviates from the linear geometric fitting showing plastic instability initiated as a notable pressure drop.

To assess the advantages and limitations of our approach, we conducted a comparative analysis, contrasting our findings with those derived from a machine-learned interatomic potentials (MLIP) based on the tabulated Gaussian approximation potential framework (tabGAP) (Byggmästar et al., 2021). The tabGAP employs the EAM-FS potentials within the training dataset, incorporating concise low-dimensional descriptors, including two-body, three-body, and an EAM-like density. In addition, the utilization of the low-dimensional descriptors facilitates the creation of more efficient tabulated versions, where MLIP energy contributions are mapped onto grids (Byggmästar et al., 2021). In Figures 2 and 3, we observed a reasonable correspondence in characterizing the transition from elastic to plastic deformation using both EAM-FS and tabGAP. However, it's important to note a distinct occurrence of the pop–in event, which falls within a range of 0.01 to 0.05 p/E_Y. This discrepancy may be attributed to the incorporation of additional surface energy information within the tabGAP framework. Additionally, our findings were compared to our prior results for Mo (Domínguez-Gutiérrez et al., 2021a, 2021b), where the use of EAM potentials with short interatomic distances corrections by the repulsive Ziegler–Biersack–Littmark (ZBL) model (Salonen et al., 2003) exhibited a higher contact pressure value at the pop-in event.

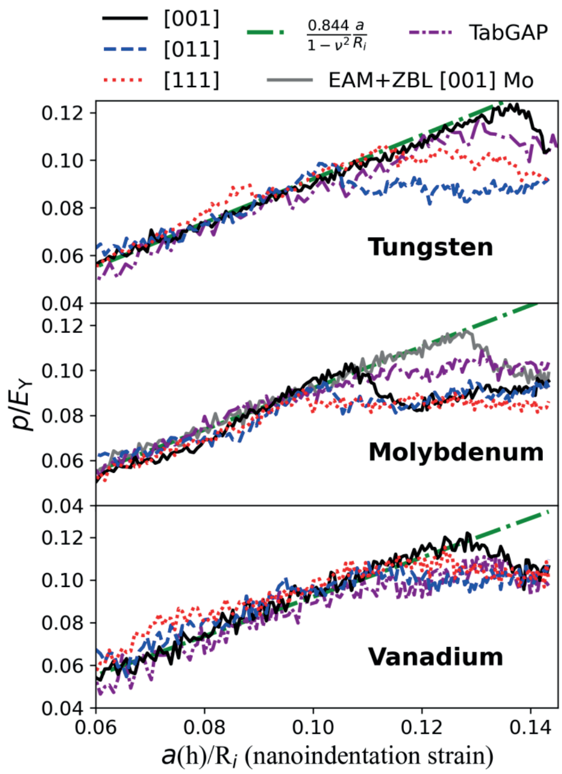

Fig. 2. Contact pressure evolution p, normalized by Young's modulus E_Y is depicted with normalized contact radius $a(h)/R_i$ for W, Mo, and V matrices. The figure employs the following color scheme: a solid black line for [001] orientation, a dashed blue line for [011], and a dotted red line for [111]. The results conform to the universal linear relationship $[0.844/(1-\nu^2)][a(h)/R_i]$, illustrated with the green dashed-dotted line. To validate our findings, comparisons with tabGAP (Byggmästar et al., 2021; Domínguez-Gutiérrez et al., 2023) for [001] samples are depicted with purple double dotted-dashed lines, and for the [001] Mo sample with EAM+ZBL simulations (Domínguez-Gutiérrez et al., 2021b; Salonen et al., 2003) represented by gray solid lines

From our MD simulations, the [001] orientation displayed the highest critical load, suggesting enhanced resistance to plastic deformation. Transitioning to the effects on Mo–W and M–V alloys, Figure 3 demonstrates the influence of Mo and V atoms in the

W matrix. For Mo, the maximum value of $p(h)/E_Y$ at [001] orientation is at 0.12 $a(h)/R_i$, between those of pure W and Mo, consistent across orientations. Also, the pressure drop is more pronounced for [001]W–Mo compared to pure W and Mo. Conversely, V atoms in W lead to decreased yield points across orientations, in agreement with the V sample but distinct from W matrices. Notably, the max($p(h)/E_Y$) for [001]W–V is 0.11 $a(h)/R_i$, lower than in pure W and V, signifying the onset of exceptional work hardening.

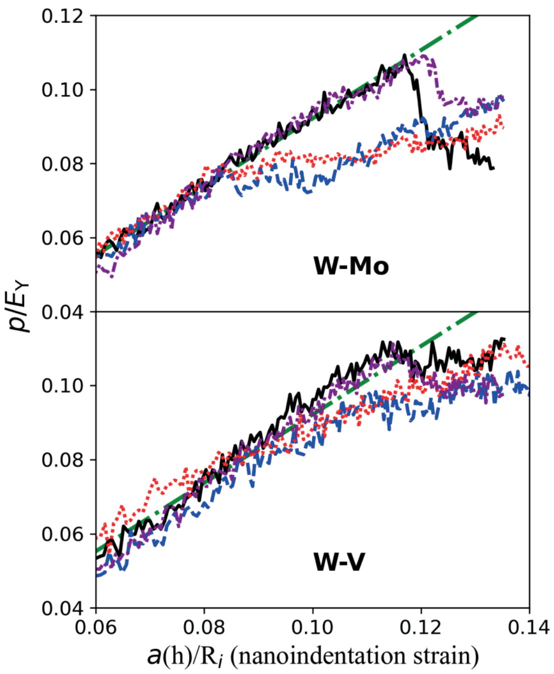

Fig. 3. Average contact pressure evolution as a function of the contact area for W–Mo and W–V alloys. TabGAP simulation results are depicted for the [001] orientation, in good agreement with EAM-FS outcomes. The color scheme is similar to the one shown in Figure 2

In our prior study (Domínguez-Gutiérrez et al., 2023), we approximated the onset of dislocation nucleation with ~0.45 – 0.5$h/a(h)$. Therefore, to estimate the maximum shear stress using contact pressure calculations, we assume an isotropic Hertzian contact model (Li T. L. et al., 2011). The maximum shear stress beneath the indenter tip (τ_{Max}) is computed as τ_{max} = 0.465max($p(h)$), where $p(h)$ is the contact pressure obtained from Figures 2 and 3 (Li T. L. et al., 2011; Xiong et al., 2016). The obtained maximum shear stress under the indenter tip for single elements (W, Mo, V) and binary alloys (W–Mo, W–V) for the [001] orientation is shown in Table 1, with EAM-FS and tabGAP results in normal and bold respectively. We used the shear modulus (G) computed using the EAM-FS potentials at 300 K to determine the maximum shear stress.

Table 1. Maximum shear stress, τ_{max} = 0.465max(p_m) (Li T. L. et al., 2011), under the indenter tip for single elements (W, Mo, V) and binary alloys (W–Mo, W–V) on the [001] crystal orientation for a strain rate of 20 m/s and 5 m/s. Additionally, the theoretical shear stress (τ_{theor} = $G/(2\pi)$) is provided, where G represents the shear modulus

	W	Mo	V	W–Mo	W–V
EAM-FS	**22.50**	**18.75**	**7.52**	**19.71**	**12.68**
TabGAP	21.61	19.20	7.06	20.06	12.02
G	136	122	43	135	84
Theor.	21.65	19.45	6.84	21.56	13.37

3.1. Dislocation network analysis

In general, dislocation glide predominantly occurs along the closest-packed ⟨111⟩ directions for BCC metals, where the Burgers vector is denoted as b = 1/2⟨111⟩. The associated slip planes are typically {110} and {112}. To analyze the atomic structure during nanoindentation tests, which provide insights into the mechanisms of dislocation nucleation and evolution (Domínguez-Gutiérrez et al., 2023), we employ OVITO (Stukowski, 2010) along with the DXA package (Stukowski et al., 2012). This approach allows us to identify dislocations, categorizing them into distinct types based on their Burgers vectors, such as the 1/2⟨111⟩, ⟨100⟩, and ⟨110⟩ dislocation types. Figure 4 shows material dislocations of selected MD simulation at maximum indentation depth for the [111] orientation, determined by the DXA method. Single-element matrices form a single dislocation loop on the {111} slip plane, along with an embryonic dislocation (Burgers vector 1/2⟨1$\bar{1}\bar{1}$⟩) traveling the {112} plane. Mo initiates a single dislocation loop and creates an embryonic dislocation on the {112} plane with the same Burgers vector. V matrices exhibit shear loop formation under the indenter, indicating plasticity. However, embryonic dislocation movement is limited, favoring lateral motion instead. This leads to a dislocation loop (Burgers vector 1/2⟨$\bar{1}\bar{1}$1⟩) followed by a second loop, typical in BCC materials (Alcalá et al., 2012).

We present results for [001] and [011] orientations in Supplementary Material of this paper, for single element materials at [001] orientation (tungsten at Fig. 4), two dislocation loops propagate within the Mo matrix, with Burgers vectors of 1/2⟨111⟩ and symmetrical ones of 1/2⟨1$\bar{1}$1⟩. In contrast, W and V samples exhibit shear loops developing toward {111} slip planes. This consistency aligns with Figure 2, where Mo maintains consistent p/E_Y values beyond 0.1$a(h)/R_i$, while others experience a contact pressure drop. For [110] orientation, W, Mo, and V matrices exhibit lasso-like mechanisms, with screw dislocations evolving Burgers vectors of $1/2\langle 1\overline{11}\rangle$ and $1/2\langle 111\rangle$, forming dislocation loops. W forms perfect loops, while Mo and V generate distorted ones due to material specific mechanical properties and Peierls barrier effects (Grigorev et al., 2023).

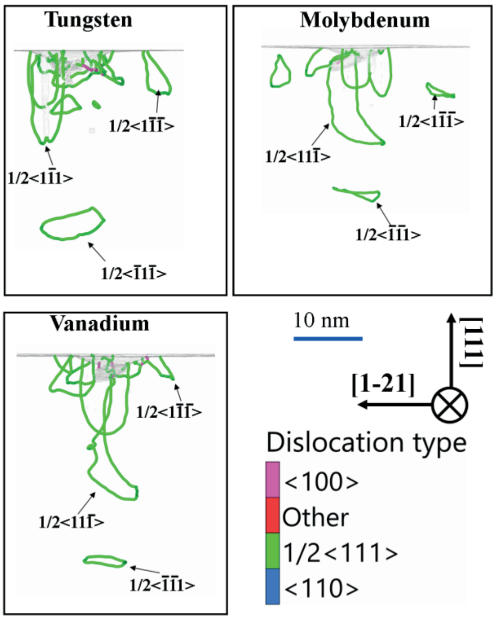

Fig. 4. Visualization of dislocations nucleated and evolved at the maximum indentation depth of 2 nm for single-element tungsten (W), molybdenum (Mo), and vanadium (V) samples on the [111] orientation. A dislocation loop with a Burgers vector of $1/2\ \langle 111\rangle$ is observed for all the samples

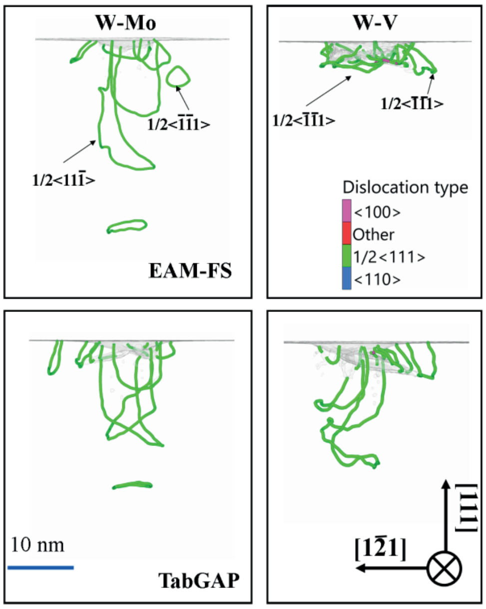

Fig. 5. Dislocation networks at the maximum indentation depth of 2 nm are portrayed for the W–Mo and W–V in alloys using EAM-FS and tabGAP approaches. A discrepancy is noticeable in the nucleation of dislocations in both approaches, stemming from the inclusion of a comprehensive training dataset for the MLIP that incorporates sufficient surface energy information

In Figure 5, the results for W–Mo and W–V alloys indicate the presence of screw dislocations, showcasing distinctive half loops encircling the indenter tip location. For W–Mo, two dislocation loops originate, while in the 50% V atoms alloy with W, screw dislocation propagation on the {111} plane notably diminishes during EAM-FS simulations. Although the MD simulations for pristine cases align with those reported by tabGAP (Domínguez-Gutiérrez et al., 2023), discrepancies arise in the W–Mo and W–V alloy analyses. While tabGAP identifies an edge dislocation loop for W–Mo, the dislocation dynamics and nucleation differ significantly in the W–V alloy. Notably, V in W matrices triggers wave-wise dislocations underneath the tip due to lattice mismatch, leading to the initiation of a loop. This variance between EAM-FS and tabGAP is due to differences in their training data, supported by DFT calculations of Peierls barrier energies (Byggmästar et al., 2022). Results for [001] and [011] orientations are depicted in the Supplementary Material.

3.2. Indented surfaces analysis

During nanoindentation loading, the indenter tip forms pile-ups and slip traces around it (Kurpaska et al., 2022; Pathak & Kalidindi, 2015), offering insight into dislocation propagation (Yu et al., 2020). To explore this, we calculate the strain tensor at maximum indentation depth using the elastic Eulerian-Almansi finite strain tensor (Stukowski et al., 2012) that describes local elastic deformation. Figure 6 displays strain field maps for [011] orientation of W in good agreement with experimental results given by Yu et al. (2020), aligning high-resolution EBSD data. Positive max strain (ϵ_{xx}) concentrates under the indenter, negative strain appears between {112} planes. ϵ_{xy} displays four-fold symmetry, ϵ_{xz} and ϵ_{yz} exhibit positive and negative poles aligned with {110} family planes, as shown by the Kikuchi wise pattern (Yu et al., 2020). In SM, we report that Mo and V exhibit similar strain patterns but with differing magnitudes due to lattice parameters and elasticity. V emphasizes strain accumulation around {110} and {112} planes in ϵ_{xx} and ϵ_{yy}. These strain maps unveil localized deformation patterns and crystallographic strain dependence in the studied materials.

In Figure 7, we illustrate strain distribution for [111] W–V alloy by EAM-FS and tabGAP. W–Mo alloy exhibits notable strain accumulation beneath the indenter tip along the {110} plane, largely in $\epsilon_{xx,y,z}$ for EAM-FS, while the tabGAP simulations show maximum values of strain on the direction of the dislocation nucleated by the applied stress.

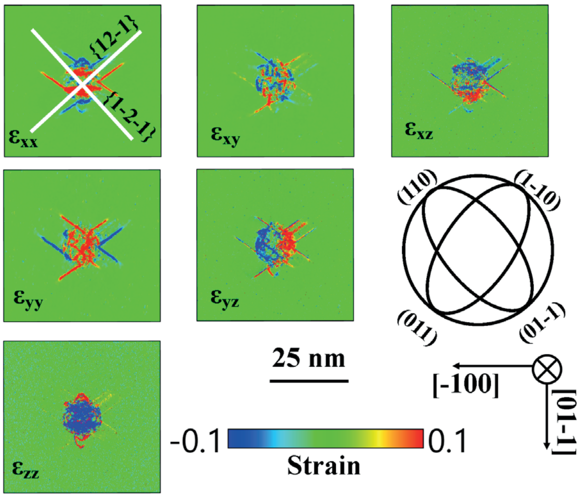

Fig. 6. Strain field mapping around the indenter tip at the maximum depth for [101]W noticing a good qualitative agreement with experimental results reported by Yu et al. (2020) and Das et al. (2018) following {112} plane families and Kikuchi wise pattern with ⟨011⟩ directions

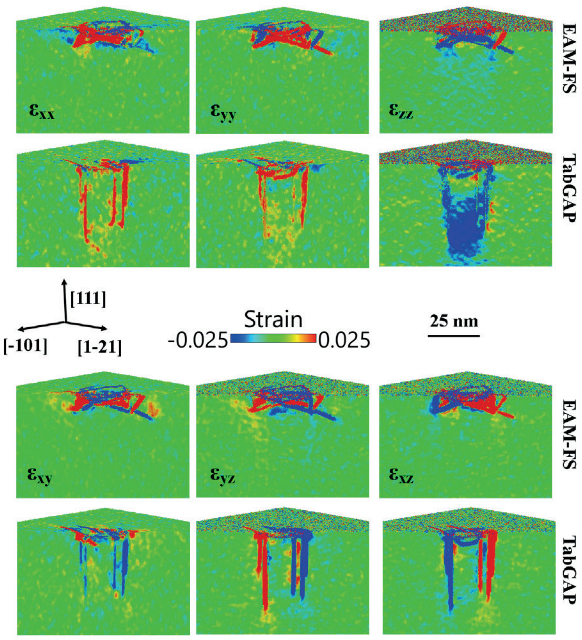

Fig. 7. Strain field mapping at the maximum indentation depth for the [101]W–V alloy using both EAM–FS and tabGAP potentials showing the difference in modeling nanomechanical during the loading process. While both approaches exhibit agreement in global calculations related to maximum shear stress, they diverge in modeling the evolution of dislocations in the W–V alloy. This difference is attributed to the more robust training data set of the tabGAP compared to the traditional EAM method, influencing their modeling of dislocation dynamics within the alloy

This arises due to V's presence in the W matrix, influencing strain and causing dislocation buildup under the tip. The strain mapping depicts dislocation evolution in this direction. In addition, strain mapping of the [111] W–V alloy indicates localized positive and negative strains under the tip, represented by $\epsilon_{xy,yz,zy}$, without significant strain propagation along crystallographic planes, as observed in tabGAP simulations. This observation suggests limited dislocation propagation within the alloy, a pattern that aligns with the representations in Figure 4. These outcomes emphasize the limitations of EAM-FS in depicting dislocation propagation, despite its strong agreement with strain-stress curves and maximum shear stress values from tabGAP. In the SM, we depict the strain mapping of the W–Mo alloy, revealing a reasonable agreement between both approaches. Understanding the distribution of strain and its dependence on crystallography is of importance for comprehending the mechanical response and deformation mechanisms present in these binary alloys.

3.3. Nanoindentation strain rate analysis

It appears that simulations conducted using the EAM-FS potential showcase good alignment with the more sophisticated MLIP methods, save for a noticeable difference in dislocation nucleation, particularly observed in the W–V alloy. However, it's important to note a substantial difference in computational wall time between these approaches. While an MD simulation using the EAM method within our computational setup, employing 120 processors, can be completed in a matter of hours, a tabGAP simulation requires several days to run due to this significant disadvantage. Consequently, to address this drawback of the tabGAP method, we opted to conduct MD simulations at a nanoindentation strain rate of 5 m/s using the EAM-FS potentials while maintaining the same numerical setup utilized for the 20 m/s case. Our primary aim is to explore the influence of strain rate on the maximum shear stress of the samples, where the EAM method exhibits strong agreement with tabGAP, except in dislocation nucleation.

Figure 8 present the results for the average contact pressure, $p_m = P_{ave}/\pi a(h)$, at a nanoindentation rate of v = 5 m/s for the single–element samples W, Mo, and V, as well as the binary alloys W–Mo and W–V for the [001] orientation, respectively (Alcalá & Esqué-de los Ojos, 2010). We observed a sudden drop in the critical contact pressure, akin to what's observed in compression mechanical tests (Papanikolaou et al., 2012, 2017; Song et al., 2019a, 2019b; Xu R.-G. et al., 2021), linked to the pop-in event during loading. Furthermore, the maximum value of p_m, signifying the initiation of plastic deformation, varied among materials. In MD simulations, the sequence of the p_m values is W, Mo, and V indicating that tungsten (W) demonstrated the highest resistance to plastic deformation. Additionally, the contact pressure decreases with decreasing nanoindentation strain rate, primarily observed in the binary alloys, consistent with experimental findings (Huo et al., 2019). This effect is due to the slower indenter tip penetration, allowing more time for dislocation evolution within the sample and shock absorption between the tip and the surface. In W–Mo alloys, the maximum value of p_m falls between that of Mo and W for both the [011] and [001] orientations, as expected. In W–V alloys, regardless of crystal orientation, this value falls between that of V and W.

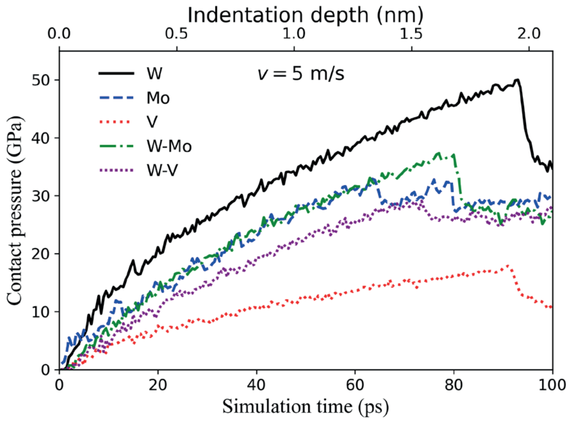

Fig. 8. The evolution of contact pressure is presented as a function of the simulation time and depth at a nanoindentation strain rate of 5 m/s for single-element W, Mo, and V matrices, and W–Mo and W–V alloys oriented along [001]. The contact pressure is averaged across 10 MD simulations for each sample, illustrating the transition from the elastic to the plastic deformation region

Table 2. Maximum shear stress, $\tau_{max} = 0.465 \max(p_m)$ (Li T. L. et al., 2011), under the indenter tip for single elements (W, Mo, V) and binary alloys (W–Mo, W–V) at different crystal orientations ([001], [011], [111]) for a strain rate of 5 m/s. Additionally, the theoretical shear stress ($\tau_{theor} = G/(2\pi)$) is provided, where G represents the shear modulus

	W	Mo	V	W–Mo	W–V
[001]	22.95	18.53	8.01	20.34	12.18
[011]	17.32	16.63	6.09	14.86	13.51
[111]	18.55	16.83	6.98	14.53	–
G	136	122	43	135	84
Theor.	21.65	19.45	6.84	21.56	13.37

In Table 2 we report results for the maximum shear stress for 5 indenter speed. We noticed that the crystallographic orientation significantly influences both the contact pressure yield point and maximum shear stress values. The τ_{Max} beneath the indenter tip is in the order of the τ_{theor} for the [001] orientations across all samples. Furthermore, the W–V alloy displayed heightened ductility for the [111] crystal orientation. This was evident in the contact pressure analysis, where the indenter tip needed to penetrate deeper into the sample to reach the yield point. Results at a rate of 20 m/s are presented in the SM.

3.4. Generalized stacking fault energies

We compute Generalized Stacking Fault Energy (GSFE) curves by considering two distinct lattice orientations that align the x–z plane with the targeted glide plane. To define the samples, we take a unit cell with lattice vectors as $\langle 112\rangle_x$, $\langle 110\rangle_y$, and $\langle 111\rangle_z$ for the {110} plane case, and $\langle 110\rangle_x$, $\langle 112\rangle_y$, and $\langle 111\rangle_z$ for the {112} plane case. These unit cells are then replicated in a 12 × 10 × 5 supercell, defining 3600 atoms with a 2.0 nm vacuum introduced at one end in the y direction to prevent interactions between periodic images (Wang et al., 2021; Xu S. et al., 2020).

The computation of each GSFE curve involves displacing the top half layers of atoms relative to the bottom half in the $\langle 111\rangle_z$ direction. Displacements occur at equal increments, with each increment representing a fraction of 0.1 of the Burgers vector magnitude. After each displacement, the top and bottom atomic layers are held fixed, while the remaining layers undergo relaxation solely in the y direction. The relaxation process, achieved through energy minimization using the conjugate gradient scheme, concludes when either (i) the quotient of the change in energy between successive iterations and the most recent energy magnitude is less than 10^{-12} or (ii) when the global force vector length of all atoms is less than or equal to 10^{-12} eV/Å (Wang et al., 2021). Then, the stacking fault energy can be calculated as (Ojha et al., 2014):

$$\gamma_{GSFE} = \frac{E_s - E_0}{A_{SF}} \tag{4}$$

where E_s represents the energy of the sample at a given displacement, and E_0 denotes the energy for the perfect sample, A_{SF} stands for the stacking fault area.

In Figure 9, the results for γ_{GSFE} on the {110} and {112} planes for pure W, Mo, and V are presented. These findings are juxtaposed with DFT calculations for W and Mo (Wang et al., 2021), and V (Zhang et al., 2017), as well as with the machine learning potential SNAP for W and Mo (Wang et al., 2021). Additionally, results for Mo using EAM+ZBL potentials (Salonen et al., 2003) are included. Notably, a commendable agreement is observed between tabGAP and DFT results for W and Mo, notwithstanding a slight discrepancy with V in the {112} plane. Regarding the EMA–FS results, it is noteworthy that the γ_{GSFE} curves are lower than those obtained through DFT, impacting the modeling of defect nucleation during the loading process.

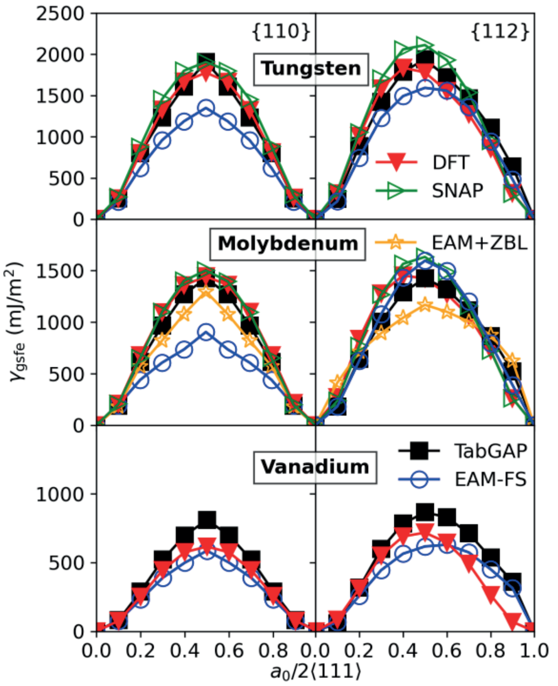

Fig. 9. Relaxed γ_{GSFE} curves on the {110} and {112} planes for pure W, Mo, and V. The presented results are compared to DFT calculations for W and Mo (Wang et al., 2021) and V (Zhang et al., 2017), as well as to other machine learning potential SNAP for W and Mo (Wang et al., 2021). Additionally, results for Mo using EAM+ZBL potentials (Salonen et al., 2003) are included. Notably, a good agreement is observed between tabGAP and DFT results

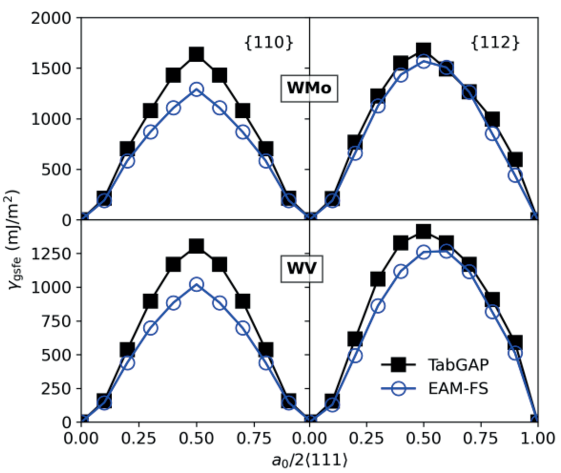

Fig. 10. Relaxed γ_{GSFE} curves are presented for the {110} plane and the {112} plane for W–Mo and W–V alloys using EAM-FS and tabGAP potentials. It is noteworthy that the energy values are consistently lower for EAM-FS compared to tabGAP, providing an explanation for the observed difference in dislocation nucleation during nanoindentation loading

In Figure 10, results for γ_{GSFE} curves for the binary alloys WMo and WV are depicted using EAM-FS and tabGAP methods. Generally, the energy values for tabGAP are higher than those presented by the EAM-FS method, particularly noticeable for the {110} plane. Notably, in the case of the W–V alloy, there is a substantial difference in energies between the two methods, especially for the {112} plane. This difference may elucidate the observed discrepancy in the nucleation of the dislocation network during the load process for the [111] W–V alloy. Specifically, the EAM-FS method requires a higher pressure for the propagation of dislocations.

4. Concluding remarks

Understanding the mechanical behavior in W-based random solution alloys is important for applications at extreme operating conditions. Our molecular dynamics simulations delved into nanoindentation responses within pure tungsten, molybdenum, vanadium, and their equiatomic W–Mo and W–V random solid solution alloys. Our analysis compared dynamic deformation, defect formation, stress-strain behaviors, and surface morphologies post-indentation. We conducted simulations employing the EAM method and explored its limitations by contrasting it with a more sophisticated, machine-learned interatomic potential within the Gaussian approximation potential (GAP) framework. These interatomic potentials are reported in the NIST database and, according to the authors' knowledge, are the only ones currently developed suitable for performing open-boundary molecular dynamics (MD) simulations for W–Mo and W–V alloys. The introduction of Mo and V into W structures reduces the Generalized Stacking Fault Energy (GSFE) values, consequently decreasing the dislocation mobility. Intriguingly, equiatomic W–V alloys displayed significant suppression of the plastic zone, indicating enhanced hardening potential compared to W-Mo counterparts. In the case of the former, we observed disparities between the EAM approach and tabGAP. EAM encountered limitations in modeling dislocation nucleation and evolution, particularly in the [111] crystal orientation. Conversely, tabGAP predicted the formation of shear loops and slower dislocation evolution. EAM indicated concentrated strain beneath the indenter tip, forming a dislocation network without effective propagation, possibly due to lower surface energies when compared to DFT calculations. Nevertheless, maximum shear stress values obtained with the EAM method are in good agreement with the theoretical results showing a crystallographic dependence for all the materials. The computed generalized stacking fault energy curves for tabGAP demonstrate a commendable agreement with ab initio calculations, particularly for the {110} plane. Additionally, they provide insights into asymmetry concerning the sense of glide direction on the {112} plane, a crucial factor contributing to the observed differences in dislocation nucleation modeling in binary alloys. Our findings suggest a promising avenue for computational material design in complex, multi-component alloys, emphasizing insights gained from small-depth nanoindentation responses.

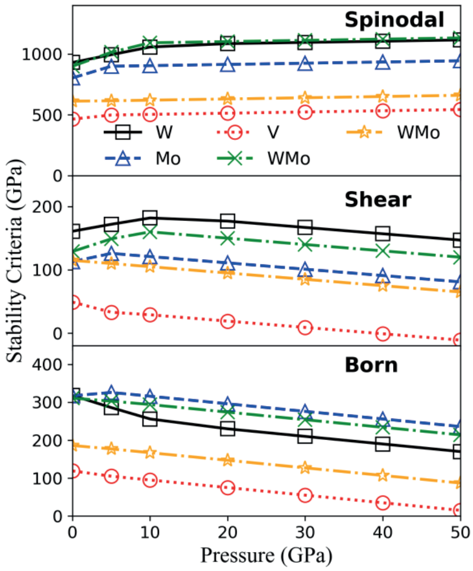

Fig. 11. Spinodal, shear, and Born stability criteria with hydrostatic pressure for single W, Mo, V, and binary alloy WMo and WV. The pressure range showing the stability of the interatomic potentials is considered to set up the numerical conditions in the MD simulations

Appendix A: Elastic stability of interatomic potentials

To validate the suitability of the EAM-FS potentials for simulations under high-stress conditions, we assess the elastic constants within a pressure range relevant to the loading process (Xiong et al., 2016). We further examine the elastic stability conditions by evaluating the spinodal, shear, and Born criteria (Xiong et al., 2014) under hydrostatic pressure P. These criteria, denoted as $M1 = C_{11} + 2C_{12} + P > 0$, $M2 = C_{44} - P > 0$, and $M3 = C_{11} - C_{12} - 2P > 0$, are shown in Figure 11. Notably, the materials exhibit stability from 0 GPa to 50 GPa, which is taken into account to set up the numerical environment for nanoindentation simulations.

Acknowledgements

We acknowledge the support of the European Union Horizon 2020 research and innovation program under grant agreement no. 857470, from the European Regional Development Fund via the Foundation for Polish Science International Research Agenda PLUS program grant No. MAB PLUS/ 2018/8, and INNUMAT project (Grant Agreement No. 101061241). We are grateful for the computational resources provided by the High Performance Cluster at the National Centre for Nuclear Research and the Interdisciplinary Centre for Mathematical and Computational Modelling (ICM) University of Warsaw under computational allocation no g91-1427.

References

Alcalá, J., & Esqué-de los Ojos, D. (2010). Reassessing spherical indentation: Contact regimes and mechanical property extractions. *International Journal of Solids and Structures*, *47*(20), 2714–2732. https://doi.org/10.1016/j.ijsolstr.2010.05.025.

Alcalá, J., Dalmau, R., Franke, O., Biener, M., Biener, J., & Hodge, A. (2012). Planar defect nucleation and annihilation mechanisms in nanocontact plasticity of metal surfaces. *Physical Review Letters*, *109*, 075502. https://doi.org/10.1103/PhysRevLett.109.075502.

Arshad, K., Zhao, M.-Y., Yuan, Y., Zhang, Y., Zhao, Z.-H., Wang, B., Zhou, Z.-J., & Lu, G.-H. (2014). Effects of vanadium concentration on the densification, microstructures and mechanical properties of tungsten vanadium alloys. *Journal of Nuclear Materials*, *455*(1–3), 96–100. https://doi.org/10.1016/j.jnucmat.2014.04.019.

Byggmästar, J., Nordlund, K., & Djurabekova, F. (2021). Modeling refractory high-entropy alloys with efficient machine-learned interatomic potentials: Defects and segregation. *Physical Review B*, *104*(10), 104101. https://doi.org/10.1103/PhysRevB.104.104101.

Byggmästar, J., Nordlund, K., & Djurabekova, F. (2022). Simple machine-learned interatomic potentials for complex alloys. *Physical Review Materials*, *6*(8), 083801. https://doi.org/10.1103/PhysRevMaterials.6.083801.

Chen, Q., Liang, S., Zhang, J., Zhang, X., Wang, Ch., Song, X., & Zhuo, L. (2020). Preparation and characterization of WMo solid solution nanopowders with a wide composition range. *Journal of Alloys and Compounds*, *823*, 153760. https://doi.org/10.1016/j.jallcom.2020.153760.

Chen, Q., Liang, S., Li, B., Chen, Z., Song, X., & Zhuo, L. (2021). Sol-gel synthesis and characterization of tungsten-molybdenum solid solution nanoparticles. *International Journal of Refractory Metals and Hard Materials*, *100*, 105668. https://doi.org/10.1016/j.ijrmhm.2021.105668.

Chen, Y., Liao, X., Gao, N., Hu, W., Gao, F., & Deng, H. (2020). Interatomic potentials of W–V and W–Mo binary systems for point defects studies. *Journal of Nuclear Materials*, *531*, 152020. https://doi.org/10.1016/j.jnucmat.2020.152020.

Das, S., Armstrong, D. E. J., Zayachuk, Y., Liu, W., Xu, R., & Hofmann, F. (2018). The effect of helium implantation on the deformation behaviour of tungsten: X-ray micro-diffraction and nanoindentation. *Scripta Materialia*, *146*, 335–339. https://doi.org/10.1016/j.scriptamat.2017.12.014.

Domínguez-Gutiérrez, F. J., Byggmästar, J., Nordlund, K., Djurabekova, F., & Toussaint, U., von (2021a). Computational study of crystal defect formation in Mo by a machine learning molecular dynamics potential. *Modelling and Simulation in Materials Science and Engineering*, *29*(5), 055001. https://doi.org/10.1088/1361-651X/abf152.

Domínguez-Gutiérrez, F. J., Papanikolaou, S., Esfandiarpour, A., Sobkowicz, P., & Alava, M. (2021b). Nanoindentation of single crystalline Mo: Atomistic defect nucleation and thermomechanical stability. *Materials Science and Engineering: A*, *826*, 141912. https://doi.org/10.1016/j.msea.2021.141912.

Dominguez-Gutierrez, F. J., Ustrzycka, A., Xu, Q. Q., Alvarez-Donado, R., Papanikolaou, S., & Alava, M. J. (2022). Dislocation nucleation mechanisms during nanoindentation of concentrated FeNiCr alloys: unveiling the effects of Cr through molecular simulations. *Modelling and Simulation in Materials Science and Engineering*, *30*(8), 085010. https://doi.org/10.1088/1361-651X/ac9d54.

Domínguez-Gutiérrez, F. J., Grigorev, P., Naghdi, A., Byggmästar, J., Wei, G. Y., Swinburne, T. D., Papanikolaou, S., & Alava, M. J. (2023). Nanoindentation of tungsten: From interatomic potentials to dislocation plasticity mechanisms. *Physical Review Materials*, *7*, 043603. https://doi.org/10.1103/PhysRevMaterials.7.043603.

Frydrych, K., Dominguez-Gutierrez, F. J., Alava, M. J., & Papanikolaou, S. (2023). Multiscale nanoindentation modelling of concentrated solid solutions: A continuum plasticity model. *Mechanics of Materials*, *181*, 104644. https://doi.org/10.1016/j.mechmat.2023.104644.

Gaffin, N. D., Ang, C., Milner, J. L., Palomares, K. B., & Zinkle, S. J. (2022). Consolidation behavior of Mo30W alloy using spark plasma sintering. *International Journal of Refractory Metals and Hard Materials*, *104*, 105778. https://doi.org/10.1016/j.ijrmhm.2022.105778.

Grigorev, P., Goryaeva, A. M., Marinica, M.-C., Kermode, J. R., & Swinburne, T. D. (2023). Calculation of dislocation binding to helium-vacancy defects in tungsten using hybrid ab initio-machine learning methods. *Acta Materialia*, *247*, 118734. https://doi.org/10.1016/j.actamat.2023.118734.

Guénolé, J., Nöhring, W. G., Vaid, A., Houllé, F., Xie, Z., Prakash, A., & Bitzek, E. (2020). Assessment and optimization of the fast inertial relaxation engine (FIRE) for energy minimization in atomistic simulations and its implementation in LAMMPS. *Computational Materials Science*, *175*, 109584. https://doi.org/10.1016/j.commatsci.2020.109584.

Gumbsch, P., Riedle, J., Hartmaier, A., & Fischmeister, H. F. (1998). Controlling factors for the brittle-to-ductile transition in tungsten single crystals. *Science*, *282*(5392), 1293–1295. https://doi.org/10.1126/science.282.5392.1293.

Huo, W., Fang, F., Liu, X., Tan, S., Xie, Z., & Jiang, J. (2019). Remarkable strain-rate sensitivity of nanotwinned CoCrFeNi alloys. *Applied Physics Letters*, *114*(10), 101904. https://doi.org/10.1063/1.5088921.

Jiang, D., Zhou, Q., Xue, L., Wang, T., & Hu, J. (2018). First-principles study the phase stability and mechanical properties of binary W-Mo alloys. *Fusion Engineering and Design*, *130*, 56–61. https://doi.org/10.1016/j.fusengdes.2018.03.050.

Jiang, D., Zhou, Q., Liu, W., Wang, T., & Hu, J. (2019). First-principles study the structures and mechanical properties of binary W-V alloys. *Physica B: Condensed Matter*, *552*, 165–169. https://doi.org/10.1016/j.physb.2018.10.005.

Johnson, K. L. (1987). *Contact Mechanics*. Cambridge University Press.

Karimi, K., Salmenjoki, H., Mulewska, K., Kurpaska, L., Kosińska, A., Alava, M. J., & Papanikolaou, S. (2023). Prediction of steel nanohardness by using graph neural networks on surface polycrystallinity maps. *Scripta Materialia*, *234*, 115559. https://doi.org/10.1016/j.scriptamat.2023.115559.

Kramynin, S. P. (2022). Theoretical study of concentration and size dependencies of the properties of Mo–W alloy. *Solid State Sciences*, *124*, 106814. https://doi.org/10.1016/j.solidstatesciences.2022.106814.

Kurpaska, L., Dominguez-Gutierrez, F. J., Zhang, Y., Mulewska, K., Bei, H., Weber, W. J., Kosińska, A., Chrominski, W., Jozwik, I., Alvarez-Donado, R., Papanikolaou, S., Jagielski, J., & Alava, M. (2022). Effects of Fe atoms on hardening of a nickel matrix: Nanoindentation experiments and atom-scale numerical modeling. *Materials & Design*, *217*, 110639. https://doi.org/10.1016/j.matdes.2022.110639.

Lan, X., Zhang, H., Li, Z.-B., & Zhang, G.-H. (2022). Preparation of fine-grained MoW solid solution alloys with excellent performances. *Materials Characterization*, *191*, 112140. https://doi.org/10.1016/j.matchar.2022.112140.

Li, T. L., Gao, Y. F., Bei, H., & George, E. P. (2011). Indentation Schmid factor and orientation dependence of nanoindentation pop-in behavior of NiAl single crystals. *Journal of the Mechanics and Physics of Solids*, *59*(6), 1147–1162. https://doi.org/10.1016/j.jmps.2011.04.003.

Li, Z., Gao, S., Brand, U., Hiller, K., & Wolff, H. (2020). A MEMS nanoindenter with an integrated AFM cantilever gripper for nanomechanical characterization of compliant materials. *Nanotechnology*, *31*(30), 305502. https://doi.org/10.1088/1361-6528/ab88ed.

Liu, G., Zhang, G. J., Jiang, F., Ding, X. D., Sun, Y. J., Sun, J., & Ma, E. (2013). Nanostructured high-strength molybdenum alloys with unprecedented tensile ductility. *Nature Materials*, *12*(4), 344–350. https://doi.org/10.1038/nmat3544.

Mulewska, K., Dominguez-Gutierrez, F. J., Kalita, D., Byggmäestar, J., Wei, G. Y., Chromiński, W., Papanikolaou, S., Alava, M. J., Kurpaska, Ł., & Jagielski, J. (2023a). Self–ion irradiation of high purity iron: Unveiling plasticity mechanisms through nanoindentation experiments and large-scale atomistic simulations. *Journal of Nuclear Materials*, *586*, 154690. https://doi.org/10.1016/j.jnucmat.2023.154690.

Mulewska, K., Rovaris, F., Dominguez-Gutierrez, F. J., Huo, W. Y., Kalita, D., Jozwik, I., Papanikolaou, S., Alava, M. J., Kurpaska, L., & Jagielski, J. (2023b). Self-ion irradiation effects on nanoindentation-induced plasticity of crystalline iron:

A joint experimental and computational study. *Nuclear Instruments and Methods in Physics Research Section B: Beam Interactions with Materials and Atoms*, *539*, 55–61. https://doi.org/10.1016/j.nimb.2023.03.004.

Muzyk, M., Nguyen-Manh, D., Kurzydłowski, K. J., Baluc, N. L., & Dudarev, S. L. (2011). Phase stability, point defects, and elastic properties of W-V and W-Ta alloys. *Physical Review B*, *84*(10), 104115. https://doi.org/10.1103/PhysRevB.84.104115.

Naghdi, A., Dominguez-Gutierrez, F. J., Huo, W. Y., Karimi, K., & Papanikolaou, S. (2022). *Dynamic nanoindentation and short-range order in equiatomic NiCoCr medium entropy alloy lead to novel density wave ordering*. arXiv. https://doi.org/10.48550/arXiv.2211.05436.

Ohser-Wiedemann, R., Martin, U., Müller, A., & Schreiber, G. (2013). Spark plasma sintering of Mo–W powders prepared by mechanical alloying. *Journal of Alloys and Compounds*, *560*, 27–32. https://doi.org/10.1016/j.jallcom.2013.01.142.

Ojha, A., Sehitoglu, H., Patriarca, L., & Maier, H. J. (2014). Twin nucleation in Fe-based bcc alloys – modeling and experiments. *Modelling and Simulation in Materials Science and Engineering*, *22*(7), 075010. https://doi.org/10.1088/0965-0393/22/7/075010.

Oliver, W. C., & Pharr, G. M. (1992). An improved technique for determining hardness and elastic modulus using load and displacement sensing indentation experiments. *Journal of Materials Research*, *7*(6), 1564–1583. https://doi.org/10.1557/JMR.1992.1564.

Papanikolaou, S., Dimiduk, D. M., Choi, W., Sethna, J. P., Uchic, M. D., Woodward, Ch. F., & Zapperi, S. (2012). Quasi-periodic events in crystal plasticity and the self-organized avalanche oscillator. *Nature*, *490*(7421), 517–521. https://doi.org/10.1038/nature11568.

Papanikolaou, S., Song, H., & Van der Giessen, E. (2017). Obstacles and sources in dislocation dynamics: Strengthening and statistics of abrupt plastic events in nanopillar compression. *Journal of the Mechanics and Physics of Solids*, *102*, 17–29. https://doi.org/10.1016/j.jmps.2017.02.004.

Pathak, S., & Kalidindi, S. R. (2015). Spherical nanoindentation stress–strain curves. *Materials Science and Engineering: R: Reports*, *91*, 1–36. https://doi.org/10.1016/j.mser.2015.02.001.

Pathak, S., Riesterer, J. L., Kalidindi, S. R., & Michler, J. (2014). Understanding pop-ins in spherical nanoindentation. *Applied Physics Letters*, *105*(16), 161913. https://doi.org/10.1063/1.4898698.

Pitts, R. A., Carpentier, S., Escourbiac, F., Hirai, T., Komarov, V., Lisgo, S., Kukushkin, A. S., Loarte, A., Merola, M., Sashala Naik, A., Mitteau, R., Sugihara, M., Bazylev, B., & Stangeby, P. C. (2013). A full tungsten divertor for ITER: Physics issues and design status. *Journal of Nuclear Materials*, *438*, S48–S56. https://doi.org/10.1016/j.jnucmat.2013.01.008.

Pöhl, F. (2019). Pop-in behavior and elastic-to-plastic transition of polycrystalline pure iron during sharp nanoindentation. *Scientific Reports*, *9*(1), 15350. https://doi.org/10.1038/s41598-019-51644-5.

Remington, T. P., Ruestes, C. J., Bringa, E. M., Remington, B. A., Lu, C. H., Kad, B., & Meyers, M. A. (2014). Plastic deformation in nanoindentation of tantalum: A new mechanism for prismatic loop formation. *Acta Materialia*, *78*, 378–393. https://doi.org/10.1016/j.actamat.2014.06.058.

Sahoo, P. K., Srivastava, S. K., Kamal, S. S. K., & Durai, L. (2015). Consolidation behavior of W–20–40 wt.% Mo nanoalloys synthesized by thermal decomposition method. *International Journal of Refractory Metals and Hard Materials*, *51*, 124–129. https://doi.org/10.1016/j.ijrmhm.2015.03.008.

Salonen, E., Järvi, T., Nordlund, K., & Keinonen, J. (2003). Effects of the surface structure and cluster bombardment on the self-sputtering of molybdenum. *Journal of Physics: Condensed Matter*, *15*(34), 5845. https://doi.org/10.1088/0953-8984/15/34/314.

Schuh, Ch. A. (2006). Nanoindentation studies of materials. *Materials Today*, *9*(5), 32–40. https://doi.org/10.1016/S1369-7021(06)71495-X.

Song, H., Dimiduk, D., & Papanikolaou, S. (2019a). Universality class of nanocrystal plasticity: Localization and self-organization in discrete dislocation dynamics. *Physical Review Letters*, *122*(17), 178001. https://doi.org/10.1103/PhysRevLett.122.178001.

Song, H., Yavas, H., Van der Giessen, E., & Papanikolaou, S. (2019b). Discrete dislocation dynamics simulations of nanoindentation with pre-stress: Hardness and statistics of abrupt plastic events. *Journal of the Mechanics and Physics of Solids*, *123*, 332–347. https://doi.org/10.1016/j.jmps.2018.09.005.

Stukowski, A. (2010). Visualization and analysis of atomistic simulation data with OVITO-the Open Visualization Tool. *Modelling and Simulation in Materials Science and Engineering*, *18*(1). https://doi.org/10.1088/0965-0393/18/1/015012.

Stukowski, A., Bulatov, V. V., & Arsenlis, A. (2012). Automated identification and indexing of dislocations in crystal interfaces. *Modelling and Simulation in Materials Science and Engineering*, *20*(8), 085007. https://doi.org/10.1088/0965-0393/20/8/085007.

Tao, H., Li, J., Li, J., Hou, Z., Yang, X., & Fan, L.-Z. (2022). Metallic phase $W_{0.9}Mo_{0.1}S_2$ for high-performance anode of sodium ion batteries through suppressing the dissolution of polysulfides. *Journal of Energy Chemistry*, *66*, 356–365. https://doi.org/10.1016/j.jechem.2021.08.026.

Thompson, A. P., Aktulga, H. M., Berger, R., Bolintineanu, D. S., Brown, W. M., Crozier, P. S., Veld, P. J., in 't , Kohlmeyer, A., Moore, S. G., Nguyen, T. D., Shan, R., Stevens, M. J., Tranchida, J., Trott, Ch., & Plimpton, S. J. (2022). LAMMPS – a flexible simulation tool for particle-based materials modeling at the atomic, meso, and continuum scales. *Computer Physics Communications*, *271*, 108171. https://doi.org/https://doi.org/10.1016/j.cpc.2021.108171.

Turchi, P., Drchal, V., Kudrnovskỳ, J., Colinet, C., Kaufman, L., & Liu, Z.-K. (2005). Application of *ab initio* and CALPHAD thermodynamics to Mo-Ta-W alloys. *Physical Review B*, *71*(9), 094206. https://doi.org/10.1103/PhysRevB.71.094206.

Varillas, J. (2019). *A Molecular Dynamics Study of Nanocontact Plasticity and Dislocation Avalanches in FCC and BCC Crystals* [Ph.D. thesis]. University of West Bohemia. https://doi.org/10.13140/RG.2.2.13904.87040.

Varillas, J., Očenášek, J., Torner, J., & Alcalá, J. (2017). Unraveling deformation mechanisms around FCC and BCC nanocontacts through slip trace and pileup topography analyses. *Acta Materialia*, *125*, 431–441. https://doi.org/10.1016/j.actamat.2016.11.067.

Wang, X., Xu, S., Jian, W.-R., Li, X.-G., Su, Y., & Beyerlein, I. J. (2021). Generalized stacking fault energies and peierls stresses in refractory body-centered cubic metals from machine learning-based interatomic potentials. *Computational Materials Science*, *192*, 110364. https://doi.org/10.1016/j.commatsci.2021.110364.

Wei, G., Byggmästar, J., Cui, J., Nordlund, K., Ren, J., & Djurabekova, F. (2023). Effects of lattice and mass mismatch on primary radiation damage in W–Ta and W–Mo binary alloys. *Journal of Nuclear Materials*, *583*, 154534. https://doi.org/10.1016/j.jnucmat.2023.154534.

Wurster, S., Gludovatz, B., Hoffmann, A., & Pippan, R. (2011). Fracture behaviour of tungsten–vanadium and tungsten–tantalum alloys and composites. *Journal of Nuclear Materials*, *413*(3), 166–176. https://doi.org/10.1016/j.jnucmat.2011.04.025.

Wyszkowska, E., Mieszczynski, C., Kurpaska, Ł., Azarov, A., Jóźwik, I., Kosińska, A., Chromiński, W., Diduszko, R., Huo, W. Y., Cieślik, I., & Jagielski, J. (2023). Tuning heterogeneous ion-radiation damage by composition in NiFe binary single crystals. *Nanoscale*, *15*, 4870–4881. https://doi.org/10.1039/D2NR06178C.

Xiong, K., Liu, X., & Gu, J. (2014). Orientation-dependent crystal instability of gamma-TiAl in nanoindentation investigated by a multiscale interatomic potential finite-element model. *Modelling and Simulation in Materials Science and Engineering*, *22*(8), 085013. https://doi.org/10.1088/0965-0393/22/8/085013.

Xiong, K., Lu, H., & Gu, J. (2016). Atomistic simulations of the nanoindentation-induced incipient plasticity in Ni_3Al crystal. *Computational Materials Science*, *115*, 214–226. https://doi.org/10.1016/j.commatsci.2015.12.045.

Xu, Q., Zaborowska, A., Mulewska, K., Huo, W., Karimi, K., Domínguez-Gutiérrez, F. J., Kurpaska, Ł., Alava, M. J., & Papanikolaou, S. (2023). Atomistic insights into nanoindentation-induced deformation of α-Al_2O_3 single crystals. *Vacuum*, *219*(A), 112733. https://doi.org/10.1016/j.vacuum.2023.112733.

Xu, R.-G., Song, H., Leng, Y., & Papanikolaou, S. (2021). A molecular dynamics simulations study of the influence of prestrain on the pop-in behavior and indentation size effect in cu single crystals. *Materials*, *14*(18), 5220. https://doi.org/10.3390/ma14185220.

Xu, S., Hwang, E., Jian, W.-R., Su, Y., & Beyerlein, I. J. (2020). Atomistic calculations of the generalized stacking fault energies in two refractory multi-principal element alloys. *Intermetallics*, *124*, 106844. https://doi.org/10.1016/j.intermet.2020.106844.

Yin, B., Maresca, F., & Curtin, W. A. (2020). Vanadium is an optimal element for strengthening in both fcc and bcc high-entropy alloys. *Acta Materialia*, *188*, 486–491. https://doi.org/10.1016/j.actamat.2020.01.062.

Yu, H., Das, S., Yu, H., Karamched, P., Tarleton, E., & Hofmann, F. (2020). Orientation dependence of the nano-indentation behaviour of pure tungsten. *Scripta Materialia*, *189*, 135–139. https://doi.org/10.1016/j.scriptamat.2020.08.014.

Zhang, X., Tang, J., Deng, L., Zhong, G., Liu, X., Li, Y., Deng, H., & Hu, W. (2017). The effects of interstitial impurities on the mechanical properties of vanadium alloys: A first-principles study. *Journal of Alloys and Compounds*, *701*, 975–980. https://doi.org/10.1016/j.jallcom.2017.01.135.